Article

Cell Systems

Torin2 Exploits Replication and Checkpoint Vulnerabilities to Cause Death of PI3K-Activated Triple-Negative Breast Cancer Cells

Graphical Abstract

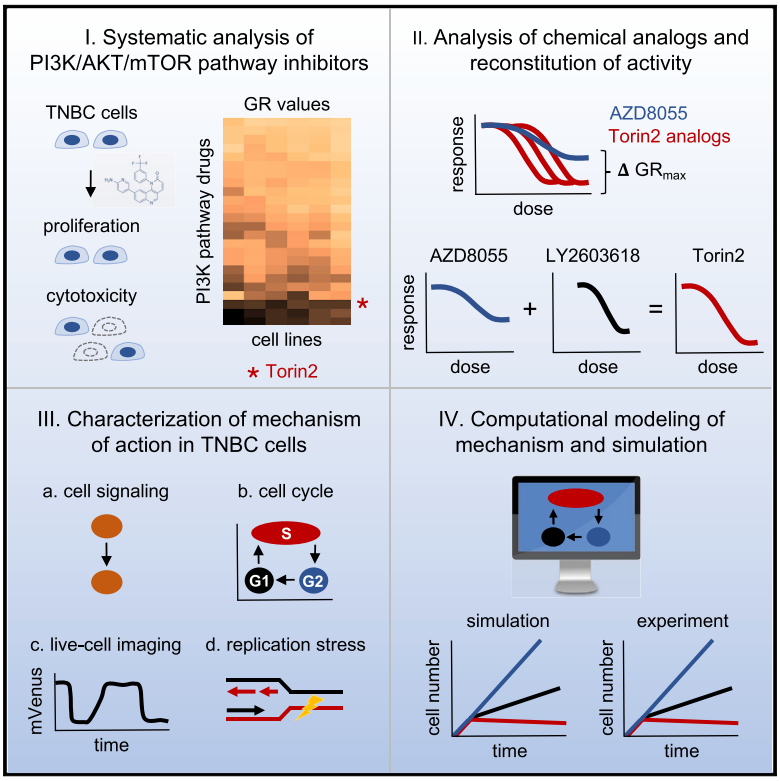

Highlights

- Torin2 causes death of TNBC cells by inhibiting several PI3K-like kinases
- Live-cell imaging shows that Torin2 exploits vulnerabilities during DNA replication
- Combined inhibition of mTOR and Chk1 with selective drugs mimics Torin2
- Computational models confirm the importance of mTOR inhibition in S phase

Authors

Sameer S. Chopra, Anne Jenney, Adam Palmer, ..., John M. Asara, Nathanael S. Gray, Peter K. Sorger

Correspondence

peter_sorger@hms.harvard.edu

In Brief

In tumors with high PI3K pathway activity, such as triple-negative breast cancer (TNBC), selective inhibitors of PI3K/AKT/mTOR pathway kinases exhibit limited efficacy as single agents. To identify possible co-targeting opportunities, we systematically analyzed responses to a compendium of PI3K/AKT/mTOR inhibitors with varying degrees of polyselectivity. We found that preclinical drugs that inhibit both mTOR and other PI3K-like kinases are more potent and effective than most clinical-grade PI3K pathway inhibitors. These polyselective mTOR inhibitors warrant further investigation as a new strategy for targeting TNBC.

Chopra et al., 2020, Cell Systems *10*, 66–81
January 22, 2020
https://doi.org/10.1016/j.cels.2019.11.001

CellPress

OPEN ACCESS
CellPress

Cell Systems
Article

Torin2 Exploits Replication and Checkpoint Vulnerabilities to Cause Death of PI3K-Activated Triple-Negative Breast Cancer Cells

Sameer S. Chopra,[1,3,5] Anne Jenney,[1,3] Adam Palmer,[1,3] Mario Niepel,[1,3] Mirra Chung,[1,3] Caitlin Mills,[1,3] Sindhu Carmen Sivakumaren,[2,5] Qingsong Liu,[2,5] Jia-Yun Chen,[1] Clarence Yapp,[1,3] John M. Asara,[4] Nathanael S. Gray,[2,5] and Peter K. Sorger[1,3,6,*]

[1]Laboratory of Systems Pharmacology, Harvard Medical School, 200 Longwood Avenue, Boston, MA 02115, USA
[2]Department of Biological Chemistry and Molecular Pharmacology, Harvard Medical School, 200 Longwood Avenue, Boston, MA 02115, USA
[3]Harvard Ludwig Center, Harvard Medical School, 200 Longwood Avenue, Boston, MA 02115, USA
[4]Division of Signal Transduction, Beth Israel Deaconess Medical Center, Harvard Medical School, 200 Longwood Avenue, Boston, MA 02115, USA
[5]Dana-Farber Cancer Institute, 450 Brookline Ave, Boston, MA 02215, USA
[6]Lead Contact
*Correspondence: peter_sorger@hms.harvard.edu
https://doi.org/10.1016/j.cels.2019.11.001

SUMMARY

Frequent mutation of PI3K/AKT/mTOR signaling pathway genes in human cancers has stimulated large investments in targeted drugs but clinical successes are rare. As a result, many cancers with high PI3K pathway activity, such as triple-negative breast cancer (TNBC), are treated primarily with chemotherapy. By systematically analyzing responses of TNBC cells to a diverse collection of PI3K pathway inhibitors, we find that one drug, Torin2, is unusually effective because it inhibits both mTOR and other PI3K-like kinases (PIKKs). In contrast to mTOR-selective inhibitors, Torin2 exploits dependencies on several kinases for S-phase progression and cell-cycle checkpoints, thereby causing accumulation of single-stranded DNA and death by replication catastrophe or mitotic failure. Thus, Torin2 and its chemical analogs represent a mechanistically distinct class of PI3K pathway inhibitors that are uniquely cytotoxic to TNBC cells. This insight could be translated therapeutically by further developing Torin2 analogs or combinations of existing mTOR and PIKK inhibitors.

INTRODUCTION

Triple-negative breast cancers (TNBCs) are high-grade, invasive mammary ductal carcinomas defined by the absence of estrogen and progesterone receptor expression and *HER2*-amplification (Foulkes et al., 2010). TNBCs are managed primarily with chemotherapy, but early disease relapse and poor overall survival underscore the need for new treatments (Foulkes et al., 2010). TNBCs have the highest inferred phosphatidylinositol 3-kinase (PI3K)/AKT/mammalian target of rapamycin (mTOR) signaling activity of all breast cancer subtypes, providing a rationale for the use of PI3K pathway inhibitors (Cancer Genome Atlas Network, 2012). High PI3K pathway activity in TNBC results both from activating mutations in *PIK3CA*, which encodes the catalytic subunit of a phosphoinositide kinase, and reduced expression of *PTEN* and *INPP4B*, which encode phosphoinositide phosphatases (Cancer Genome Atlas Network, 2012). PI3K pathway kinases have been targeted with >40 small-molecule drugs but clinical responses to date have been modest (Janku et al., 2018). PI3K pathway drugs are non-selective for transformed cells, which also limits their therapeutic index (Chia et al., 2015). Isoform-selective PI3K inhibitors are better tolerated but only sporadically active in solid tumors, possibly due to insufficient pathway inhibition or feedback mechanisms that cause pathway reactivation (Elkabets et al., 2013; Schwartz et al., 2015).

One way to overcome such limitations is to combine PI3K pathway inhibitors with other drugs or exploit the polyselectivity of existing molecules (André et al., 2019; Knight et al., 2010). Whereas many PI3K pathway drugs inhibit several PI3K isoforms and/or mTOR, some also inhibit other PI3K-like kinases (PIKKs) because of structurally similar ATP binding sites. For example, the PI3K-mTOR inhibitor dactolisib (NVP-BEZ235) and the active-site mTOR inhibitors Torin1 and Torin2, which antagonize the activities of mTOR complex 1 (mTORC1) and mTOR complex 2 (mTORC2), also inhibit ataxia telangiectasia and Rad3-related (ATR), ataxia telangiectasia mutated (ATM), and/or DNA-dependent protein kinase, catalytic subunit (DNA-PKcs) (Liu et al., 2010, 2013; Toledo et al., 2011). This unique polyselectivity may be particularly relevant to TNBC because of frequent alterations in *TP53*, *MYC*, and *CCNE1*, which cause increased dependency on PIKKs due to defective DNA damage checkpoints and increased replication stress (Cancer Genome Atlas Network, 2012; Lin et al., 2017; Zeman and Cimprich, 2014).

In this paper, we analyzed the responses of TNBC cells with an activated PI3K pathway to a diverse collection of PI3K pathway

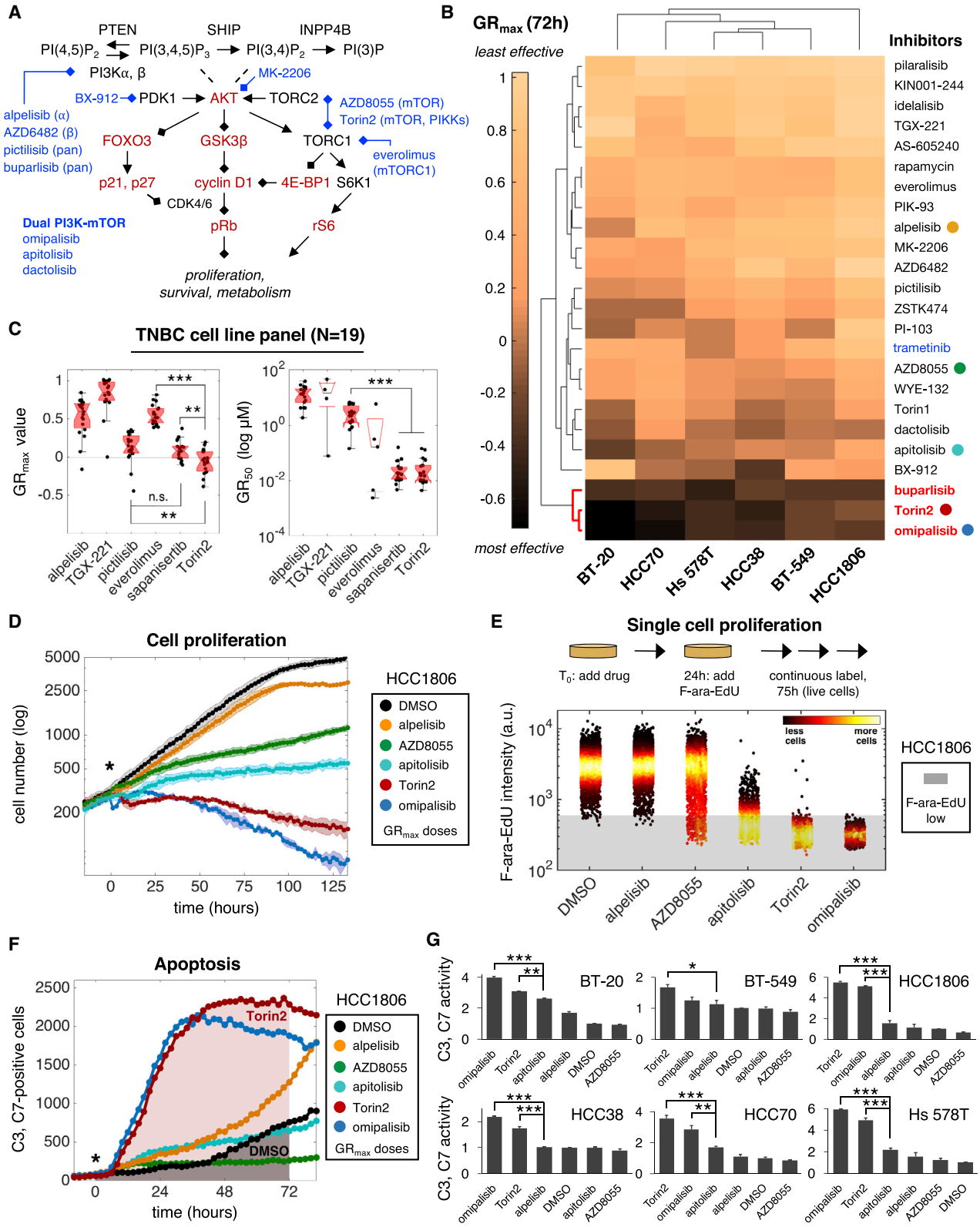

Figure 1. Torin2 Produces Strong Cytotoxic and Anti-proliferative Effects in TNBC Cells

(A) Schematic of the PI3K pathway with select drugs (blue) and measured proteins (red).

(B) Clustergram heatmap of mean GR_{max} values for 24 drugs in six TNBC cell lines; n = 3 experiments. Dark shading denotes $GR_{max} < 0$ (i.e., cytotoxicity). Red, highly effective drugs; blue, MAPK inhibitor. Colored circles mark drugs analyzed in (D)–(G).

(legend continued on next page)

inhibitors. We found that most drugs neither fully block proliferation nor cause cell death. In contrast, the preclinical compound Torin2 induced apoptosis in all cell lines tested. To determine which of the four high-affinity targets of Torin2 is responsible, we used a chemical genetic approach involving dose-response studies in multiple cell lines, analysis of chemical analogs, and pharmacological reconstitution with mixtures of selective inhibitors. Phenotypes were determined using single-cell, time course, and pulse-labeling assays. These studies show that inhibition of both mTOR and other PIKKs is responsible for the high activity of Torin2 in TNBC. Thus, co-targeting several PIKKs with a single polyselective drug or a mixture of selective compounds makes it possible to exploit replicative and checkpoint vulnerabilities unique to TNBCs to promote selective cell killing.

RESULTS

Torin2 Produces Strong Cytotoxic and Anti-proliferative Effects in TNBC Cells

Breast cancer cell lines are classified as basal or luminal based on gene expression (Neve et al., 2006). We performed western blotting on 46 cell lines and found that those with basal-like gene expression had uniformly low levels of PTEN and/or INPP4B (Figure S1A; Table S1); five such lines were selected for compound screening (HCC1806, Hs 578T, HCC38, BT-549, and HCC70). A sixth basal line (BT-20) with an activating *PIK3CA* mutation (H1047R) but normal levels of PTEN and INPP4B was also screened. All six lines lack hormone receptor expression and *HER2* amplification and are homozygous for *TP53* mutations (Table S2). We assembled a diverse panel of 23 PI3K pathway inhibitors that included clinically approved drugs, investigational agents, and tool compounds; the MEK inhibitor trametinib served as a mitogen-activated protein kinase (MAPK)-pathway-specific comparator (Figure 1A; Table S3). Sub-confluent cultures were treated for 72 h with each drug at nine doses and viable cells counted by microscopy at time t = 0 and 72 h (Figure S1B). Dose-response data were analyzed using growth rate inhibition (GR) metrics, which quantify drug sensitivity while correcting for differences in cell division times (T_d) (Hafner et al., 2016): GR_{50} is analogous to the half maximal inhibitory concentration (IC_{50}) and measures potency, while GR_{max} is analogous to the maximal drug effect (E_{max}) and measures efficacy (Figure S1C). A value of $GR_{max} < 0$ indicates a net cell loss, a value of zero represents no change in viable cell number, and a value > 0 indicates a net cell gain. By convention, $GR_{max} = 1$ in control cultures, which were treated with DMSO only.

Highly effective responses (i.e., negative GR_{max} values) were rare across the 144 drug-cell line combinations examined (Figure 1B), but three drugs were broadly cytotoxic: the phase 3 PI3K p110 pan-isoform inhibitor buparlisib, the phase 1 PI3K-mTOR inhibitor omipalisib, and the preclinical mTOR-PIKK inhibitor Torin2. Omipalisib and Torin2 were also highly potent, with nanomolar GR_{50} values (Figure S1D). Torin2 is the least studied molecule of the three, but we found it to be more cytotoxic in 19 basal-like cell lines than sapanisertib, an active-site mTOR inhibitor presently in clinical trials (Figure 1C). Torin2 exhibited similar efficacy to sapanisertib in luminal breast cancer cell lines (n = 7) and caused little or no cytotoxicity in non-malignant mammary epithelial cells (n = 2) (Figure S1E). Thus, Torin2 may represent an improved way to target TNBC.

To identify factors influencing drug response, we assayed proliferation and apoptosis in live cells. To enable a principled comparison, compounds were used at the lowest concentration eliciting a GR_{max} response (i.e., the "GR_{max} dose"). We imaged HCC1806 cells expressing a nuclear localization sequence fused to mCherry (NLS-mCherry) continuously for >5 days (~4.5 cell divisions; T_d = 28 h) in the presence of DMSO or several drugs whose GR_{max} values span a broad range. Drugs with positive GR_{max} values, such as the PI3Kα inhibitor alpelisib (GR_{max} = 0.92), the active-site mTOR inhibitor AZD8055 (GR_{max} = 0.56), and the PI3K-mTOR inhibitor apitolisib (GR_{max} = 0.37), reduced viable cell number but did not fully block proliferation (Figure 1D). Conversely, drugs with negative GR_{max} values such as Torin2 ($GR_{max} = -0.16$) and omipalisib ($GR_{max} = -0.29$) steadily reduced cell number. At a 10-fold lower dose (0.32 μM) of Torin2 or omipalisib, there was still no increase in cell number over time, consistent with complete cytostasis or a balance between cell division and death (Figure S1F).

As another measure of proliferation, we exposed HCC1806 cells to drugs for 24 h and then added (2′*S*)-2′-deoxy-2′-fluoro-5-ethynyluridine (F-ara-EdU), a non-toxic thymidine analog that is incorporated into newly synthesized DNA, for an additional 75 h (2.7 × T_d) (Neef and Luedtke, 2011). GR_{max} doses of alpelisib, AZD8055, and apitolisib were only partly effective at inhibiting F-ara-EdU labeling, resulting in 0.7%, 6.3%, and 65.4% unlabeled cells; in contrast, Torin2 and omipalisib each inhibited the labeling of >99% of viable cells (Figures 1E and S1G). Thus, the low GR_{max} values of Torin2 and omipalisib are associated with fewer cells that actively synthesize DNA during drug exposure.

To assay apoptosis, we exposed six cell lines to drugs in the presence of a fluorogenic substrate of executioner caspases 3 and 7 (C3 and C7) and measured substrate cleavage by imaging (Figure S1H). We then calculated the fold change in the area under the fluorescence curve (AUC) between 0 and 72 h relative to a DMSO control (Figures 1F and 1G). Drugs such as AZD8055 induced no detectable C3 and/or C7 activity in any cell line. In contrast, Torin2 and omipalisib increased C3 and/or C7 activity

(C) GR_{max}, GR_{50} values in 19 TNBC cell lines. **p < 0.01, ***p < 0.001, and n.s. (not significant) by Mann-Whitney U test.
(D) Growth curves for HCC1806 NLS-mCherry cells. "*" denotes the start of the treatment. Data points and shading depict mean ± SD of 3 replicates in a representative time-lapse experiment; n = 3 experiments.
(E) Mean nuclear F-ara-EdU intensity values in HCC1806 cells after treatment for ~100 h; n = 3 experiments, representative data shown. "a.u." indicates arbitrary units. Shading indicates unlabeled cells.
(F) C3 and/or C7-positive cell counts over time as detected by live-cell imaging of HCC1806 cells. Shading indicates AUC for 72 h of drug exposure.
(G) C3 and/or C7 activity (i.e., mean fold change in AUC ± SEM for drug versus DMSO); n = 2 experiments. *p < 0.05, **p < 0.01, ***p < 0.001 by one-way ANOVA and Tukey's test (selected comparisons shown). Drugs were used at GR_{max} doses (1–3.2 μM) in (D)–(G), with exceptions as noted in STAR Methods.
See also Figure S1 and Tables S1–S3.

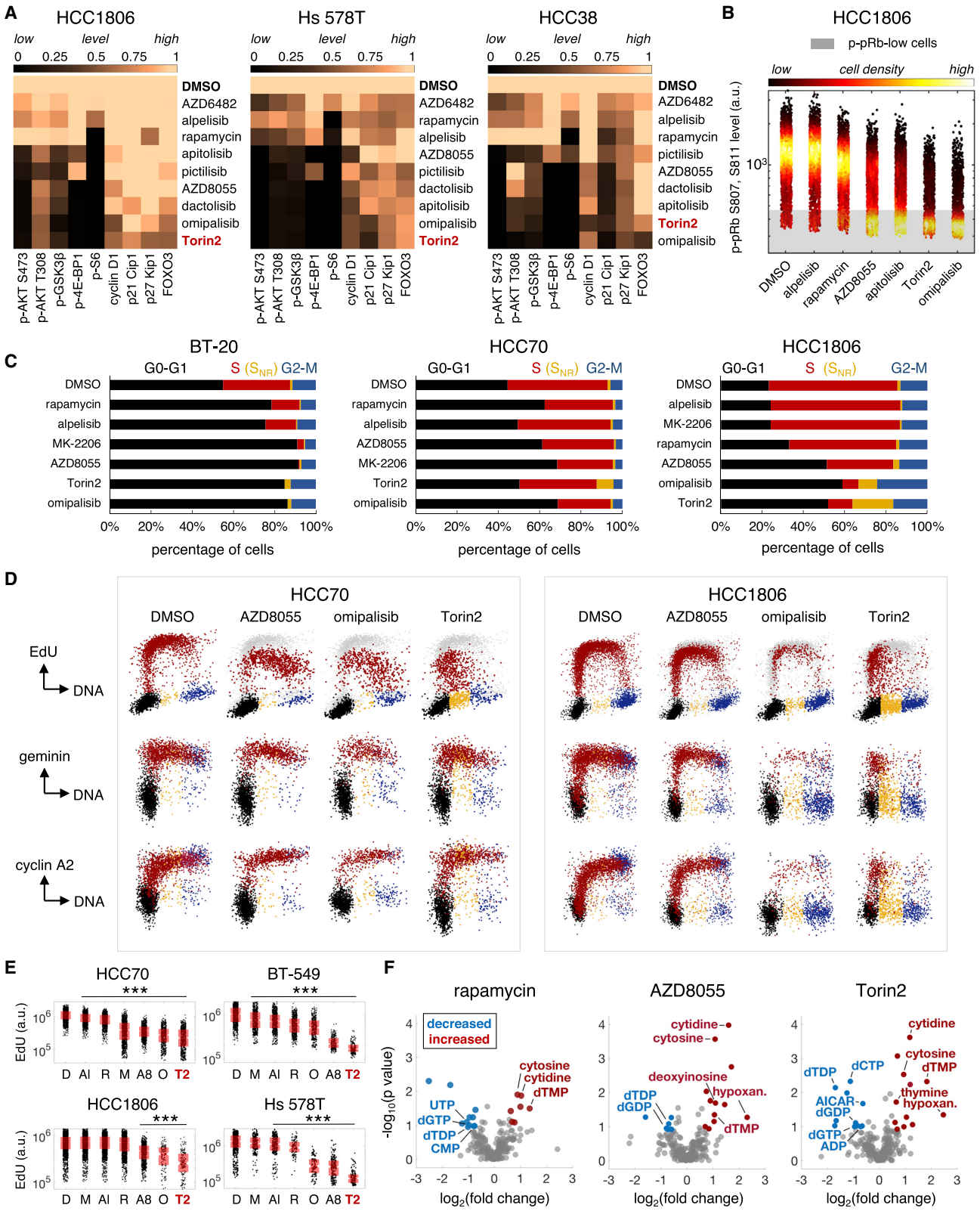

Figure 2. PI3K/AKT/mTOR Inhibitors Impede Progression of S Phase

Drugs were used at GR_{max} doses (1–3.2 μM) throughout, with exceptions as noted in STAR Methods. (A) Clustergram heatmaps rank the activity of PI3K pathway drugs based on levels and/or localization of nine proteins/phosphoproteins at 24 h. Data normalized to DMSO; n ≥ 2 experiments.

(legend continued on next page)

by an average of ~3.5-fold across all six lines. Overall, these data show that low GR_{max} values for Torin2 and omipalisib in TNBC cells result from effective inhibition of proliferation and induction of apoptosis.

PI3K/AKT/mTOR Inhibitors Impede Progression of S Phase

To evaluate the effects of Torin2 on signaling, we exposed TNBC cells to GR_{max} doses of drugs for 24 h and then quantified the levels or localization of nine proteins or phosphoproteins by immunofluorescence microscopy (Figures 1A, 2A, and S2A–S2C). AKT activity was inferred from (1) phosphorylation at T308 and S473, (2) phosphorylation of GSK-3β at S9, and (3) nuclear localization of FoxO3. The activities of mTORC1, mTORC2, and S6K1 were assayed by phospho-4E-BP1 T37 and/or T46, phospho-AKT S473, and phospho-S6 S235 and/or S236. We also measured levels of cyclin D1, p21, and p27, which are regulated by the PI3K pathway. Based on changes in these proteins/phosphoproteins, Torin2 and omipalisib were found to be the most effective PI3K pathway inhibitors (Figures 2A and S2D). To assay the "output" of the PI3K pathway, we quantified CDK-dependent phosphorylation of retinoblastoma protein (p-pRb) on S807 and/or S811. When mitogenic signaling is low, CDK activity is also low, pRb is dephosphorylated, and E2F is inhibited, causing G1 arrest (Duronio and Xiong, 2013). In HCC1806 cells, exposure to Torin2 or omipalisib for $t = T_d$ increased the percentage of p-pRb-low cells from 5% to 64% and 81%, compared to 6%–42% for six other PI3K pathway drugs (Figures 2B and S2E). Thus, low GR_{max} values for Torin2 and omipalisib correlate with greater suppression of PI3K signaling and lower levels of p-pRb (Liang and Slingerland, 2003).

To determine if Torin2 inhibits cell-cycle progression at the G1-to-S phase transition to a greater extent than other PI3K pathway drugs, we stained DNA with Hoechst and pulse-labeled S-phase cells with EdU (Figure S3A). Cell lines with different T_ds were compared by exposing cells to drugs for $t = T_d$ and then labeling with EdU for $0.025 \times T_d$ (40–70 min). EdU-positive cells were scored as being in S phase and EdU-negative cells scored as being in G0 or G1 (G0-G1) or G2 or mitosis (G2-M) based on DNA content. EdU-negative cells with a DNA content intermediate between G0-G1 and G2-M cells were scored as S-phase-non-replicating (S_{NR}) cells (Shi et al., 2001).

Exposure of BT-20 cells to $0.3 \times GR_{max}$ dose (1 μM) of Torin2 or omipalisib for $t = T_d$ (48 h) increased the G0-G1 fraction to ~85% (from 55% in DMSO control) and reduced the S-phase fraction to 0% (from 33% in DMSO control; Figure 2C). In contrast, GR_{max} doses of drugs less effective than Torin2 at suppressing PI3K pathway activity (i.e., alpelisib and rapamycin) increased the G0-G1 fraction to a lesser degree (76%–79%) and incompletely reduced the S-phase fraction (to 13%–15%). Thus, in *PIK3CA*-mutant TNBC cells, the high activities of Torin2 and omipalisib are associated with an increased blockade of cells in G0-G1 and elimination of S-phase cells.

In contrast, exposure of other cell lines to Torin2 or omipalisib, even at doses that blocked proliferation, did not eliminate S-phase cells (Figures 2C and S3B). For example, 26%–41% of HCC70 cells were in S phase after exposure to Torin2 or omipalisib for $t = T_d$ (45 h). To determine if this phenotype arises because Torin2 and other PI3K pathway drugs impede progression of cells through S phase, we quantified the amount of EdU incorporated into DNA during pulse labeling. To identify S-phase cells independent of DNA synthesis, we measured levels of expression of the anaphase-promoting complex/cyclosome-Cdh1 (APC) substrates geminin and cyclin A2 by immunofluorescence. In HCC70 cells, multiple PI3K pathway drugs reduced EdU content in geminin- and cyclin A2-positive cells (Figures 2D and 2E). Torin2 suppressed DNA synthesis to the greatest degree and caused accumulation of S_{NR} cells (~9% of all cells). In HCC1806 cells, Torin2 elicited even stronger inhibition of S phase, with accumulation of >20% of S_{NR} cells (Figures 2D, 2E, S3C, and S3D). These S_{NR} cells exhibited decreased levels of geminin, cyclin A2, and p-pRb, consistent with cell-cycle exit (Figures 2D and S3E). PI3K pathway drugs also reduced EdU content in BT-549 and Hs 578T cells, with Torin2 again having the strongest effect (Figures 2E, S3F, and S3G). The same was true for BT-20 cells exposed to drugs for a less time ($t = 0.125–0.3 \times T_d$; 6–14 h), substantially earlier than the G0-G1 arrest that occurred by $t = T_d$ (Figures S3H and S3I). Thus, Torin2 and other PI3K pathway drugs not only inhibit the cell cycle at the G1-to-S phase transition but also interfere with progression of S phase.

The PI3K pathway is known to play a role in nucleotide metabolism (Wang et al., 2009). We therefore hypothesized that exposure of TNBC cells to PI3K pathway drugs impedes S phase by decreasing levels of DNA precursors (Juvekar et al., 2016). To test this idea, we performed targeted metabolomic profiling by mass spectrometry following a short exposure of BT-549 cells to one of three mTOR inhibitors (rapamycin, AZD8055, or Torin2) or DMSO for $t = 0.15 \times T_d$ (6 h). Drug-exposed cells exhibited changes in levels of multiple purine and pyrimidine deoxyribonucleotides and their precursors, consistent with inhibition of both *de novo* synthesis and salvage pathways (Figure 2F; Table S4). Torin2 elicited the largest number of changes, but all three drugs elicited higher levels of cytidine and cytosine, key substrates in the salvage of pyrimidines. The drugs also increased levels of deoxythymidine monophosphate (dTMP) and decreased levels of deoxythymidine diphosphate (dTDP), consistent with reduced

(B) Mean nuclear intensity values of p-pRb S807, S811 in HCC1806 cells at $t = T_d$ (28 h).
(C) Cell-cycle distributions at $t = T_d$ for BT-20 (48 h), HCC70 (45 h), and HCC1806 (28 h) based on analysis of DNA versus EdU content. Colors: G0-G1, black; S phase, red; S-phase non-replicating (S_{NR}), yellow; and G2-M, blue. Drugs are ordered from least to most effective (top to bottom) based on viable cell counts.
(D) Top row: DNA versus EdU content at $t = T_d$. Data points for DMSO appear in background (gray); colors indicate different cell-cycle stages as in (C). Middle, bottom rows: DNA versus mean nuclear intensity of geminin or cyclin A2. Colors indicate different cell-cycle stages determined by DNA and EdU content values measured in the same cells.
(E) Quantification of total nuclear EdU content in gated S-phase cells (red cells, top row in D; S_{NR} cells excluded). Al, alpelisib; A8, AZD8055; D, DMSO; M, MK-2206; O, omipalisib; R, rapamycin; and T2, Torin2. ***$p < 0.001$ for each drug versus DMSO (Mann-Whitney U test).
(F) Changes in intracellular polar metabolites after exposure of BT-549 cells to drugs for $t = 0.15 \times T_d$ (6 h). Nucleotides and precursors are labeled.
See also Figures S2 and S3 and Table S4.

activity of deoxythymidylate kinase, an enzyme that acts downstream of both *de novo* pyrimidine synthesis and salvage pathways. Thus, it is likely that Torin2 and the other drugs we tested inhibit S-phase progression at least in part by depleting TNBC cells of nucleotides required for DNA replication.

Torin2 Causes Substantial Cell Killing during S-G2 Phases

To better understand how Torin2 acts on cells in different cell-cycle stages, we performed time-lapse imaging of asynchronous HCC1806 cells stably expressing H2B-mTurquoise and mVenus-hGeminin(1–110) (Sakaue-Sawano et al., 2008). Cells were exposed to DMSO or 0.3 × GR_{max} dose (1 μM) of omipalisib or Torin2 and then followed for 48 h (n = 340 single cells tracked and analyzed, Figure 3A). H2B-mTurquoise was used to identify nuclei, monitor cell division, and score cell death by nuclear fragmentation. Cell-cycle stage was determined by the fluorescence intensity level of mVenus, which is low in G1 and high in S and G2 (S-G2). In the presence of DMSO, single cells divided every 24.2 ± 0.8 h, consistent with measured population doubling times, and only ~6% died (Figure 3A). Exposure to omipalisib caused the death of 38% of cells (n = 43/112) and blocked progression of 55% (n = 61/112); the remainder of the cells were incompletely blocked (Figures 3A and 3B). Torin2 was more cytotoxic, killing 51% of cells (n = 62/122) and blocking progression of 43% (n = 53/122).

Confirming data obtained from fixed cells, live-cell imaging showed that Torin2 and omipalisib are active during both G1 and S-G2 phases of the cell cycle. In the presence of omipalisib, a similar numbers of cells died in S-G2 (44%; n = 19/43) as in G1 (56% of cells; n = 24/43) (Figures 3A and 3B). In contrast, 8-fold more cells exposed to Torin2 died in S-G2 (89% of cells, n = 55/62) than in G1 (11%, n = 7/62). Among surviving cells, Torin2 also imposed a stronger S-G2 block than omipalisib: 30% of blocked cells (n = 16/53) were in S-G2 after exposure to Torin2 compared to only 2% (n = 1/61) for omipalisib. The strong effects of Torin2 on S-G2 cells caused the sequence of events leading to G1 block or death to differ between the two drugs. For example, the majority of omipalisib-treated cells that died in G1 (66.7%, n = 16/24) or remained blocked there (65%, n = 39/60) were in S-G2 at the time of drug exposure; they then proceeded through mitosis to the following G1 where they either died or arrested (G1 "class 2" death or block, Figures 3C and 3D). In contrast, G1 class 2 deaths (57.1%, n = 4/7) and block (40.5%, n = 15/37) were less frequent in the presence of Torin2 because the majority of cells in S-G2 at the time of initial drug exposure never reached mitosis. We conclude that both Torin2 and omipalisib are active on cells in G1 and S-G2 but that exposure to Torin2 causes substantially greater arrest and death of S-G2 cells than omipalisib.

Torin2 Causes Replication Catastrophe

Impaired S-phase progression by nucleotide insufficiency or other genotoxic insults is a cardinal manifestation of "replication stress" (Zeman and Cimprich, 2014). Stalled replication forks cause accumulation of single-stranded DNA (ssDNA) because the activities of DNA polymerases and replicative helicases become uncoupled; excess ssDNA can then consume replication factors and cause DNA breakage and death by "replication catastrophe" (Toledo et al., 2013). To determine if exposure to Torin2 causes accumulation of ssDNA, HCC1806 cells were labeled with 5-bromo-2'-deoxyuridine (BrdU) for t = T_d, treated with GR_{max} doses of the drug for t = 0.2 × T_d (5 h), and immunostained with anti-BrdU antibodies under non-denaturing ("native") conditions. Exposure to Torin2, but not to omipalisib or AZD8055, increased the fraction of cells with elevated ssDNA ~8-fold (Figure 4A, labeled red, and Figure 4C) and mean nuclear BrdU intensity in gated S-phase cells ~2-fold (Figure 4B). Similar increases were observed with AZ20 and rabusertib, selective inhibitors of ATR and its substrate checkpoint kinase 1 (Chk1), which act together to stabilize stalled replication forks and suppress origin firing (Zeman and Cimprich, 2014). Exposure of HCC1806 cells to Torin2, AZ20, and rabusertib also increased levels of phosphorylated H2A.X S139 (γH2A.X), a marker of DNA damage, and of the phosphorylated form of the ssDNA-binding protein RPA (p-RPA) modififed on S4 and/or S8 (Figures 4A–4C). Similar effects were seen in HCC70 cells but after longer periods of drug exposure (~0.5 × T_d, 24 h) (Figures S4A and S4B). In HCC1806 cells, these responses were associated with activated intra-S-phase checkpoint signaling, as evidenced by a ~15-fold increase in the fraction of cells with elevated phosphorylated Chk1 (p-Chk1) S317 and phosphorylated Chk2 (p-Chk2) T68 (Figures 4C and S4C). In contrast, neither AZD8055 nor omipalisib caused any detectable increase in ssDNA, γH2A.X, p-RPA, p-Chk1, or p-Chk2, despite inhibiting DNA synthesis. Thus, Torin2 is unique among the PI3K pathway drugs we tested in causing accumulation of ssDNA, DNA damage, and increased checkpoint signaling in TNBC cells.

To determine whether increased ssDNA and DNA damage precede accumulation of S_{NR} cells and death, HCC1806 cells were exposed to Torin2 at 0.3 × GR_{max} dose (1 μM) for 0.2–1.7 × T_d (5–48 h). At 5, 11, 24, or 48 h, cells were pulse labeled with EdU for 0.025 × T_d (40 min) and counterstained with anti-γH2A.X antibodies. Between 5 and 48 h of drug exposure, ~50%–60% of EdU-positive cells were positive for γH2A.X, a >10-fold increase over cells exposed to DMSO for 5 h (Figure 4D). Over the same time period, the fraction of EdU-negative cells that were γH2A.X-positive increased from 1% to 54%, these cells had DNA content values characteristic of S_{NR} cells (Figure 4E). Torin2 exposure was similar to rabusertib exposure in generating S_{NR} cells with homogeneous, pan-nuclear γH2A.X staining, thereby demonstrating severe genotoxic stress and commitment to apoptosis (de Feraudy et al., 2010) (Figure 4F). No such staining pattern was observed after cells were exposed to omipalisib. Overall, more than 50% of S-phase HCC1806 cells exposed to Torin2 for 5–48 h exhibited pan-nuclear γH2A.X staining, and similar effects were observed in other TNBC cell lines (Figures 4G and 4H). Thus, ssDNA and DNA damage induced by Torin2 precede the appearance of S_{NR} cells exhibiting hallmarks of replication catastrophe.

The Activity of Torin2 Results from Combined Inhibition of mTOR and Other PIKKs

To test the hypothesis that the activity of Torin2 on TNBC cells results from its unique polypharmacology, we attempted to reconstitute Torin2-induced phenotypes in HCC1806 and HCC70 cells by combining selective inhibitors of mTOR and other PIKKs. The combination of AZD8055 and rabusertib

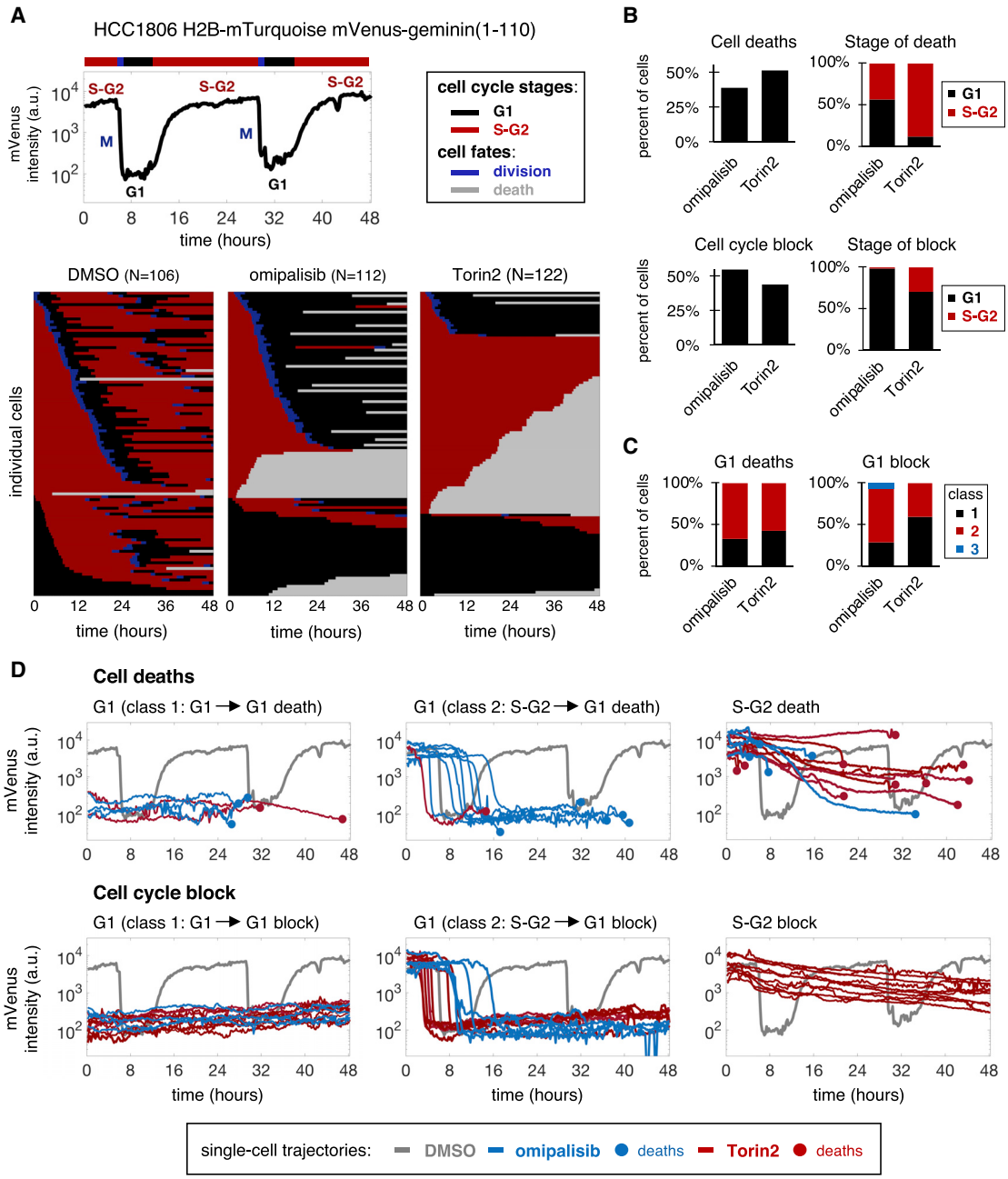

Figure 3. Torin2 Causes Substantial Cell Killing during S-G2 Phases

(A) Time-lapse imaging of asynchronous HCC1806 cells expressing H2B:mTurquoise and mVenus:hGeminin(1–110). mTurquoise was used to score cell division and death and mVenus intensity levels were used to identify cell-cycle stage, as illustrated for a representative DMSO-exposed cell. Heatmaps show the progression of 340 cells through the cell cycle after exposure to DMSO or a 0.3 × GR_{max} dose (1 μM) of omipalisib or Torin2 for 48 h. Colors denote cell-cycle stages and cell fates (see legend).

(B) Frequency of deaths and cell-cycle block (left) and distribution by cell-cycle stage (right).

(C) Frequencies of response classes leading to G1 death or block, based on cell-cycle stage at the time of drug exposure. Class 1, a cell in G1 is killed or blocked in the same G1; class 2, a cell in S-G2 divides but the daughter cell is killed or blocked in the following G1; and class 3, similar to class 2, except the parental cell starts in G1.

(D) Phenotypic responses caused by drug exposure. Shown are representative traces of mVenus fluorescence intensity versus time for single cells treated with omipalisib (blue) or Torin2 (red). The trace for a DMSO-exposed cell is shown in the background (gray) for comparison.

most closely matched the activity of Torin2 across a range of doses (Figures 5A and S5A), possibly because inhibition of Chk1 mimics the inhibition of both ATR and DNA-PKcs (Buisson et al., 2015). AZD8055 combined with either rabusertib or AZ20 was more effective (by GR_{max}) than inhibiting mTOR alone and more potent (by GR_{50}) than inhibiting ATR or Chk1 alone. In a

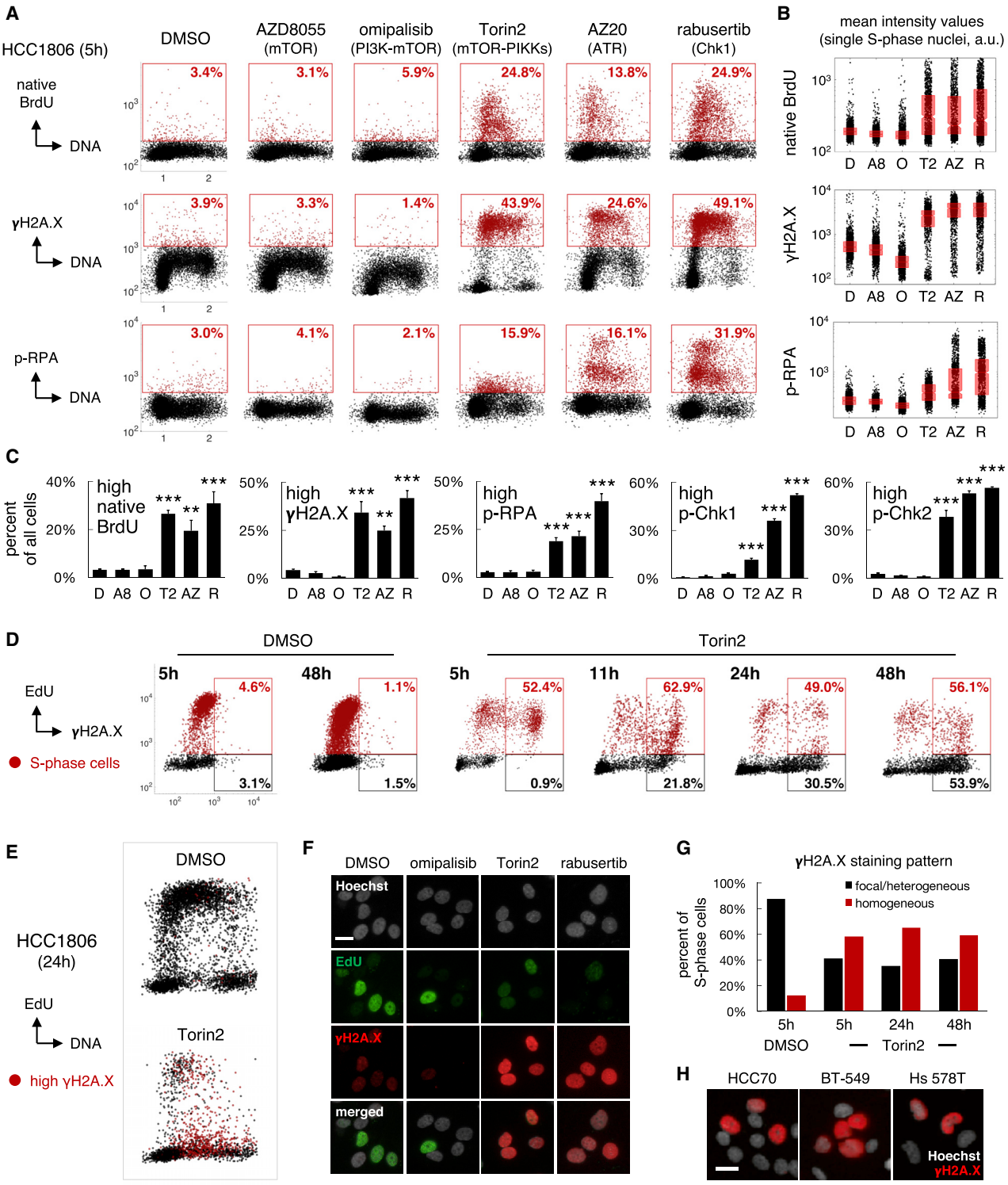

Figure 4. Torin2 Causes Replication Catastrophe

HCC1806 cells were exposed to 0.3–1 × GR_{max} drug doses (1–3.2 μM) throughout.

(A) DNA content versus intensities of native BrdU, γH2A.X, or p-RPA after drug exposure for ~0.2 × T_d (5 h). Cells with high levels are gated (red). Percentages are of all cells.

(B) Quantification of nuclear intensity values in gated S-phase cells. Boxplots show median and 25th to 75th percentiles. D, DMSO; A8, AZD8055; O, omipalisib; T2, Torin2; AZ, AZ20; and R, rabusertib.

(legend continued on next page)

complementary approach, we compared AZD8055 to nine Torin2 analogs (Figure S5B) and Torin1, which inhibits mTORC1/2 and DNA-PK but not ATR or ATM (Liu et al., 2010). Most Torin2 analogs were less potent than AZD8055 and Torin1 but were more effective (i.e., negative GR_{max} values, Figures 5B and 5C).

To dissect the relative contribution of inhibiting mTOR or other PIKKs to the activity of Torin2 analogs, we exposed HCC1806 and HCC70 cells to a 100-fold concentration range of each drug for t = 0.33–0.5 × T_d (14 h) and assayed mTOR signaling activity by immunofluorescence microscopy of p-AKT S473 and p-4E-BP1 T37 and/or 46. We found that the magnitude of mTOR inhibition at 14 h correlated well with GR values at 72 h for multiple drugs and analogs, including Torin1 and AZD8055 (Figures 5D and S5C, black regression lines). However, at low levels of mTOR signaling activity, the GR values for Torin2 (red circles), QL-VI-86 (#5), QL-V-107 (#6), QL-IV-100 (#7), and QL-VIII-58 (#8) were substantially lower, resulting in a discontinuous relationship between mTOR inhibition and GR values (Figures 5D and S5C, red lines or boxes). Thus, mTOR inhibition alone does not fully account for the high activity of these drugs. This same subset of drugs caused elevated pan-nuclear staining of γH2A.X in S-phase cells, consistent with inhibition of additional PIKKs (Figures 5D–5G and S5C–S5E). In HCC1806 cells, these drugs also elicited an increase in the fraction of p-pRb-low cells in G1, S, and G2-M phases, indicative of arrest at multiple points in the cell cycle (Figures 5E, black lines beneath scatterplots, and 5F). We conclude that Torin2 and its analogs exhibit more or less of two distinct cellular activities. Whereas all compounds inhibit mTOR and cause growth inhibition, a subset of compounds including Torin2 also inhibit additional PIKKs to cause DNA damage and cytotoxicity. The most effective drugs are those with the strongest combined activity.

Combined Inhibition of mTOR and ATR or Chk1 Is Beneficial because Multiple Pathways Required for S Phase Are Co-targeted

The high activity of Torin2 and its analogs is unexpected. In principle, G0-G1 arrest caused by inhibiting mTOR should antagonize cell death in S phase (or M) from inhibiting other PIKKs such as ATR (Johnson et al., 1999; King et al., 2015). To better understand why Torin2 and its analogs are so effective, we developed two cell-cycle models based on discrete time-step Monte Carlo simulations. In these models, single cells progressed through G1, S, G2, and M "compartments" at rates matching experimental data. Following M phase, each mother cell was replaced by two G1 daughters. In the "independence model," mTOR inhibition slowed transit only through G1, while in the "interaction model," mTOR inhibition slowed transit through both G1 and S phase (Figures 6A and 6B). In both models, ATR or Chk1 inhibition caused replication block and S- or M-phase lethality. GR values and total cell killing ("cell loss factor") were then calculated for simulations with different degrees of mTOR and ATR or Chk1 inhibition.

When the rate of cell killing caused by ATR or Chk1 inhibition was low (between 0 and 0.15 in Figure 6C), the independence model predicted greater cytostasis with increased mTOR inhibition. However, with higher cytotoxicity (values of 0.2 to 0.3), blocking mTOR had an antagonistic effect. A kinetic simulation of submaximal doses of an ATR or a Chk1 inhibitor combined with an mTOR inhibitor demonstrated only a modest effect on viable cell number (Figure 6D). In contrast, the interaction model predicted substantially decreased GR values and increased cell killing across a wide range of activities of ATR or Chk1 and mTOR inhibitors (Figure 6E). Antagonism between mTOR and ATR or Chk1 inhibitors was observed only at the highest levels of mTOR inhibition, which markedly prolonged G1. Kinetic simulations of submaximal drug activities acting in combination yielded growth curves with negative slopes, denoting cytotoxicity (Figure 6F). Thus, the interaction model demonstrates that mTOR inhibitors causing an incomplete block at the G1-to-S phase transition can be beneficially combined with ATR or Chk1 inhibitors if the two drugs increase the probability of S- or M-phase cell killing. The cytotoxic effects of Torin2 and its analogs are thus likely to depend on the sensitivity of TNBC cells to inhibition of both mTOR and other PIKKs during S phase.

To test experimentally whether combinations of PI3K/AKT/mTOR and ATR or Chk1 inhibitors are beneficial or antagonistic, we performed isobologram analysis on two-way dose-response landscapes for 16 different combinations—eight PI3K/AKT/mTOR inhibitors versus an ATR or a Chk1 inhibitor—in five TNBC cell lines. Each of the 80 landscapes involved 100 different dose ratios. Using Loewe criteria (Tallarida, 2011), we classified combinations as exhibiting independence or favorable or antagonistic interactions (Figure 6G). In total, 46 out of 80 combinations exhibited pharmacological interaction, of which 45 (98%) were at least additive and only one was antagonistic (Figures 6H and S6A). As predicted by modeling, favorable drug interactions gave rise to increased cell killing at submaximal concentrations of PI3K pathway inhibitors that only partly suppress mTOR signaling and incompletely block proliferation (Figures 6I, S6B, and S6C). In HCC70 cells, for example, low doses of AZD8055 (0.03 × GR_{max}, 0.1 μM) were sufficient to delay progression of S phase; when combined with low doses of rabusertib (0.1 × GR_{max}, 0.32 μM), we observed significantly greater suppression of EdU incorporation in mid- and late S-phase cells compared to either drug alone (Figures 6J and 6K). Thus, as predicted by the interaction model, several PI3K pathway drugs can be combined

(C) Mean percent ± SEM of cells with high levels of the indicated markers; n = 3 experiments. **p < 0.01, ***p < 0.001 versus DMSO by one-way ANOVA and Dunnett's test.
(D) Mean nuclear intensity of EdU versus γH2A.X after treatment with DMSO or 1 μM Torin2 for the indicated times. EdU and γH2A.X double-positive cells (red gate) and EdU-negative, γH2A.X-positive cells (black gate) are quantified as a percent of all EdU-positive (red) or EdU-negative (black) cells.
(E) DNA versus mean EdU intensity at 24 h post-treatment with DMSO or 1 μM Torin2. Cells with γH2A.X > 10^3 a.u. are red.
(F) Pan-nuclear γH2A.X staining pattern in S-phase and S_{NR} cells at 24 h post-treatment with 1 μM of drugs.
(G) Percent of S-phase cells with pan-nuclear γH2A.X (red) versus focal (black) staining after exposure to DMSO or 1 μM Torin2.
(H) γH2A.X staining pattern in various TNBC cell lines after treatment with 1 μM Torin2. Scale bars, 20 μm in (F) and (H).
See also Figure S4.

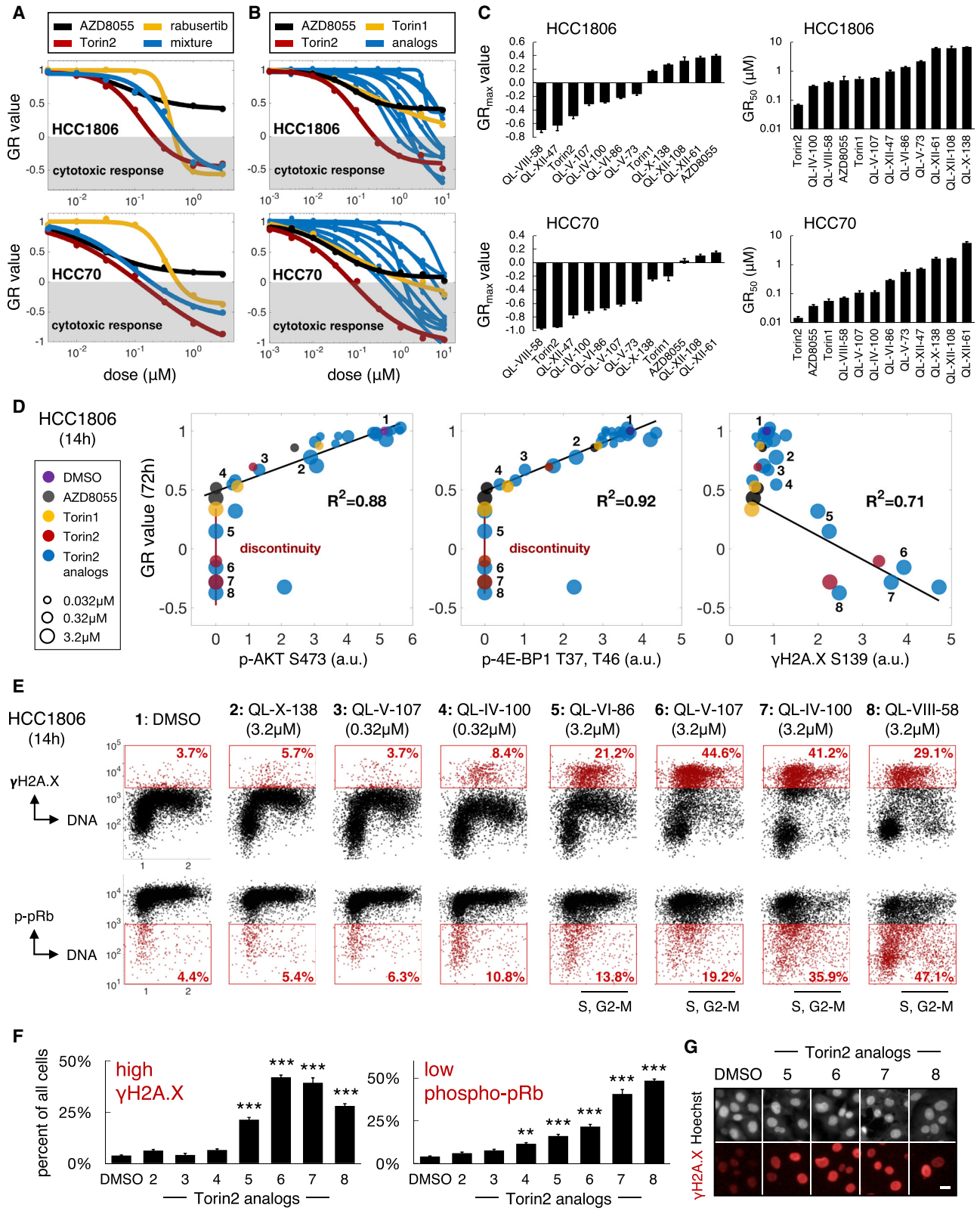

Figure 5. The Activity of Torin2 Results from Combined Antagonism of mTOR and other PIKKs

(A) 72 h dose-response curves; "mixture" denotes equimolar concentrations of AZD8055 and rabusertib.

(B) 72 h dose-response curves; "analogs" indicate Torin2 chemical analogs.

(legend continued on next page)

with an ATR or a Chk1 inhibitor to produce a benefit in TNBC cell lines.

Low Doses of an mTOR Inhibitor and a Chk1 Inhibitor in Combination Cause Increased ssDNA in Mitotic Prophase and Death

Exposure of HCC70 cells to low doses of AZD8055 and rabusertib in combination strongly suppressed DNA synthesis but did not cause the accumulation of S_{NR} cells observed in other lines (i.e., HCC1806). We therefore asked whether low-dose combinations increase cell killing by a mechanism distinct from replication catastrophe, such as by causing cells with incompletely replicated DNA to inappropriately enter mitosis (King et al., 2015). To investigate this possibility, we studied early mitotic (prophase) cells in asynchronous drug-treated cultures, as identified by positive staining for phospho-histone H3 (p-HH3) S10 and uncondensed chromatin (visualized by Hoechst staining). To detect ssDNA, cells were labeled with BrdU for t = T_d and stained with anti-BrdU antibodies under native conditions (Figure 7A). We found that exposure of HCC70 cells to the combination of 0.03 × GR_{max} AZD8055 (0.1 μM) and 0.1 × GR_{max} rabusertib (0.32 μM) for t = 0.5 × T_d (24 h) produced higher fractions of BrdU-positive prophase cells and higher nuclear BrdU intensity levels than either drug alone or than a 0.3 × GR_{max} dose (1 μM) of Torin2 (Figures 7B–7D). Thus, the low-dose combination causes increased mitotic entry of HCC70 cells with ssDNA.

To determine the fates of these cells, we stained chromosomes, centromeres, spindle fibers, and centrosomes using Hoechst and anti-CREST, anti-β-tubulin, and anti-γ-tubulin antibodies, following drug exposure for t = 0.5 × T_d (24 h). While AZD8055 alone decreased the total number of mitotic figures per high-powered field, rabusertib and the low-dose combination increased mitotic cell counts by 1.7- and 2.6-fold, respectively (n = 672 fields; $p < 0.001$ for combination versus rabusertib by one-way ANOVA and Tukey's test) (Figure S7A). The combination also increased the percentage of mitotic cells in metaphase to 80%, compared to 28% for DMSO, 36% for AZD8055 alone, and 58% for rabusertib alone (n = 569 mitotic cells; $p < 0.01$ for combination versus rabusertib) (Figure S7B). More than 90% of metaphase cells treated with AZD8055 plus rabusertib exhibited fragmented and/or misaligned chromosomes (n = 188 metaphase cells; $p < 0.01$ for combination versus rabusertib for severe misalignment and $p < 0.05$ for chromosome fragmentation) (Figures 7E and 7F). Thus, cells with high levels of ssDNA are delayed in metaphase with incorrectly aligned or damaged chromosomes.

The interdependency of these events was made more obvious by time-lapse imaging of cells expressing H2B-GFP. Drug-induced abnormalities in chromatin condensation visible in prophase frequently led to aberrant metaphases (n = 198 and 222 cells tracked through mitosis at 15 and 30 h, respectively) (Figure 7G). Mitotic death ensued after varying lengths of time without evidence of progression to anaphase. Although the rate of mitotic entry was lower in cells treated with the low-dose combination versus rabusertib alone (0.8% versus 1.7% of cells per hour after 30 h of drug exposure; Figure S7C), nearly 80% of cells entering mitosis in the presence of the drug combination underwent mitotic catastrophe (a 2.2-fold increase over rabusertib alone) (Figure 7H). Of all drug-treated cells that died during mitosis, >97% failed between prophase and metaphase. We conclude that low doses of an mTOR inhibitor and a Chk1 inhibitor in combination can cause high rates of mitotic failure in some TNBC cell lines.

DISCUSSION

The frequency of mutations in PI3K pathway genes in human cancers has motivated development of numerous small-molecule kinase inhibitors (Janku et al., 2018), few of which are effective in patients. We find that the preclinical compound Torin2 is unusually active in blocking proliferation and inducing death of PI3K-activated TNBC cells. In contrast, Torin2 is only partially cytostatic in non-transformed mammary epithelial cells. Torin2 was developed as an active-site mTOR inhibitor, but reconstitution experiments and analysis of chemical analogs both show that its activity in TNBC results from combined inhibition of mTOR and other PIKKs. In multiple TNBC lines, combinations of drugs targeting mTOR and ATR or Chk1 also show favorable effects. Thus, the polyselectivity of Torin2 is essential for its high activity in TNBC.

The benefits of combining mTOR and ATR or Chk1 inhibitors are unexpected because the two drug classes primarily affect successive cell-cycle stages. PI3K/AKT/mTOR signaling canonically regulates the G1-to-S phase transition (Liang and Slingerland, 2003), while ATR-Chk1 is required during S phase and at the G2-M checkpoint (Zeman and Cimprich, 2014). Prior studies have shown that combinations of chemotherapies or chemotherapy plus radiation are antagonistic when successive cell-cycle stages are affected (Johnson et al., 1999; Sui et al., 2004). This is intuitive because cells blocked in G1 cannot proceed into later phases of the cell cycle where cytotoxicity occurs. However, in TNBC cells, we find that PI3K pathway drugs also disrupt progression of S phase. Modeling and experimentation together suggest that combinations of mTOR and ATR or Chk1 inhibitors can produce a benefit under conditions in which mTOR inhibition incompletely blocks cells in G1 and yet slows the rate of replication in S phase. Thus, the relative insensitivity of TNBC cells to the anti-proliferative effects of mTOR inhibitors

(C) Mean ± SEM of GR_{max}, GR_{50} values for drugs in (B); n = 3 experiments.
(D) Levels of p-AKT, p-4E-BP1, and γH2A.X in HCC1806 cells at t = 0.5 × T_d (14 h) of drug exposure versus GR values (72 h) for 0.032–3.2 μM of drugs in (B). Black regression lines show drugs and doses whose GR values correlate with decreased mTOR signaling (left and middle) or increased γH2A.X (right). Red lines show drugs/doses discontinuous with the regression.
(E) DNA versus nuclear γH2A.X or p-pRb levels in HCC1806 cells at 14 h of exposure to DMSO or numbered drugs in (D). Gates indicate cells with high or low levels; percentages are of all cells.
(F) Mean percent ± SEM of data in (E); n = 3 experiments. **$p < 0.01$, ***$p < 0.001$ by one-way ANOVA and Dunnett's test.
(G) Nuclear γH2A.X staining pattern in HCC1806 cells after exposure to Torin2 analogs for 14 h. Numbers as in (D)–(F). Scale bar, 20 μm.
See also Figure S5.

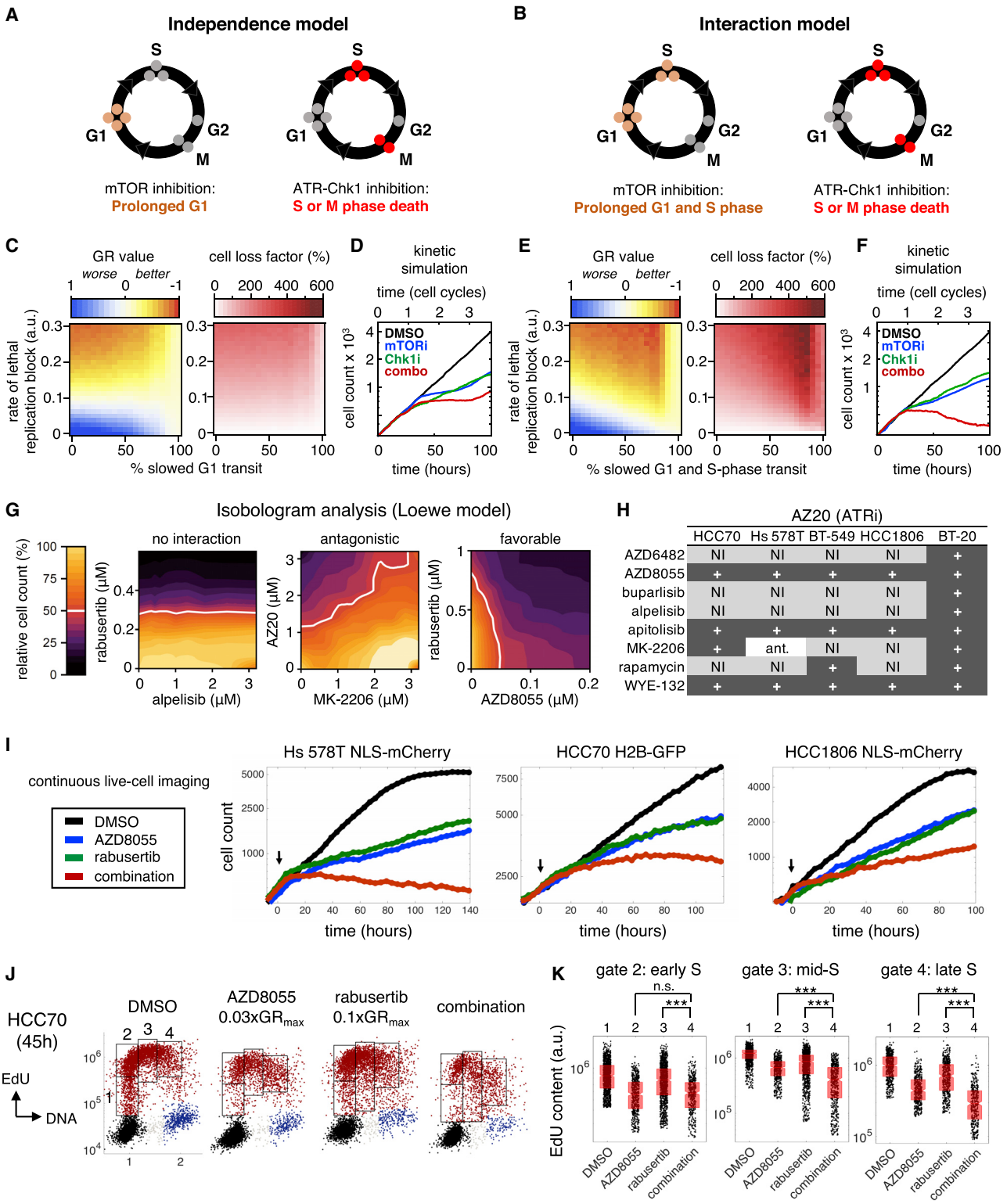

Figure 6. Combined Inhibition of mTOR and ATR or Chk1 Produces Benefit by Co-targeting Pathways Required in S Phase

(A) Schematic of the independence model.

(B) Schematic of the interaction model.

(C) Simulated GR values and cell loss factor (cytotoxicity) for the independence model, in which mTOR inhibition prolongs G1 and ATR or Chk1 inhibition causes lethality in S phase or mitosis, as a consequence of replication block.

(legend continued on next page)

at G1-S is a liability for monotherapy but an opportunity for combination therapies that exploit vulnerabilities in S phase. The strong effects of Torin2 on S-phase cells appear to result from a felicitous combination of reduced rates of DNA synthesis due to mTOR inhibition and reduced replication fork stability due to inhibition of additional PIKKs. The accumulation of ssDNA and DNA damage caused by exposure to Torin2 consequently results in the death of TNBC cells in S phase or subsequent mitosis.

We find that reduced rates of DNA synthesis following exposure to PI3K pathway inhibitors are associated with altered levels of nucleotides and their precursors. Short exposure of TNBC cells to mTOR inhibitors causes increased levels of cytidine and cytosine, which are known substrates for pyrimidine salvage pathways, as well as changes in the levels of dTDP and dTMP consistent with reduced activity of deoxythymidylate kinase, an enzyme required for pyrimidine synthesis. Prior studies have found that PI3K pathway activity promotes metabolic flux through the non-oxidative arm of the pentose phosphate pathway to generate ribose 5-phosphate and phosphoribosylpyrophosphate (PRPP), which are required for purine and pyrimidine synthesis (Juvekar et al., 2016; Wang et al., 2009). Moreover, mTORC1 regulates the activity of CAD, which catalyzes *de novo* pyrimidine synthesis, and expression of *MTHFD2*, which increases *de novo* purine biosynthesis (Ben-Sahra et al., 2013, 2016). In addition to causing metabolic derangements, mTOR inhibitors may also impede S-phase progression by reducing transcription and translation of proteins required for DNA replication and repair (Silvera et al., 2017).

Dependencies on ATR-Chk1 signaling for S-phase progression are also likely to be multifactorial in origin (Zeman and Cimprich, 2014). Oncogenes commonly amplified in TNBC such as *MYC* and *CCNE1* cause excessive origin firing and conflicts between replication and transcription, resulting in stalled replication forks (Macheret and Halazonetis, 2018). Because of the uncoupling of replicative helicases and DNA polymerases, stalled forks generate ssDNA and activate ATR-Chk1 signaling (Zeman and Cimprich, 2014). In the presence of replication stress, ATR or Chk1 inhibition causes accumulation of ssDNA, consumption of replication factors, DNA damage, and "replication catastrophe" (Toledo et al., 2013). Loss-of-function mutations in *TP53* may also contribute to this outcome, since absence of the DNA damage checkpoint in G1 renders cells more dependent on ATR-Chk1 signaling for the function of alternative cell-cycle checkpoints to maintain genomic integrity (Ma et al., 2011). By inhibiting both mTOR and other PIKKs, Torin2 effectively exploits S-phase and checkpoint vulnerabilities in TNBC to promote tumor cell killing.

Translational Prospects

The foremost challenge in targeting the PI3K pathway for anti-cancer therapy is achieving anti-proliferative effects and cell killing sufficient to block tumor growth at doses tolerated by patients. The PI3K-mTOR inhibitor omipalisib is emblematic of this challenge: omipalisib produces substantial growth inhibition and apoptosis in TNBC cell lines, but the maximum tolerated dose in patients fails to fully inhibit intratumoral AKT and has only modest antitumor activity (Munster et al., 2016). To improve the therapeutic index, recent efforts have focused on the development of selective inhibitors of PI3K p110 isoforms (α, β, δ, and γ), but these drugs often lack sufficient activity in solid tumors as monotherapy (Costa et al., 2015; Elkabets et al., 2013; Schwartz et al., 2015). Thus, the polyselectivity of Torin2-like compounds appears promising in that it eliminates the requirement for strong inhibition of mitogenic signaling and G1 arrest to produce efficacy. We have also shown that certain PI3K pathway inhibitors can be used at relatively low doses in combination with other drugs to exploit replicative and/or checkpoint vulnerabilities and produce cytotoxicity. Thus, new combinatorial strategies inspired by Torin2 may not only be more effective but also have a greater therapeutic index in patients.

STAR★METHODS

Detailed methods are provided in the online version of this paper and include the following:

- KEY RESOURCES TABLE
- LEAD CONTACT AND MATERIALS AVAILABILITY
  - Materials Availability Statement
- EXPERIMENTAL MODEL AND SUBJECT DETAILS
  - Cell Lines
  - Cell Line Generation
- METHOD DETAILS
  - Western Blotting
  - Evaluation of Drug Sensitivity
  - Drug Dosing
  - Immunofluorescence Microscopy
  - Primary Antibodies and Dilutions
  - Single-Stranded DNA (ssDNA) and Cell-Cycle Analysis
  - Live-Cell Microscopy
  - Extraction of Polar Metabolites
  - Metabolomics Profiling by Targeted Mass Spectrometry
  - Isobolograms and Analysis of Drug Interactions
  - Cell-Cycle Model and Simulation of Combinatorial Drug Effect

(D) Simulated growth curves for the independence model.
(E) Identical simulations as in (C) but for the interaction model, in which mTOR inhibition prolongs both G1 and S phase.
(F) Simulated growth curves for the interaction model.
(G) Examples of no interaction, antagonism, or favorable drug interaction by isobologram analysis. The white line indicates 50% reduced viable cell count.
(H) Summary of interactions between PI3K pathway drugs and the ATR inhibitor AZ20. "+" indicates additive or greater benefit by Loewe criteria, "N.I." indicates no interaction (independence) and "ant." indicates antagonism.
(I) Live-cell imaging of cells treated with sub-GR_{max} doses of AZD8055 and/or the Chk1 inhibitor rabusertib. Doses for each cell line (AZD8055 and rabusertib): Hs 578T (0.1 and 0.5 μM); HCC70 (0.032 and 0.32 μM); and HCC1806 (0.320 and 0.32 μM).
(J) DNA content versus EdU content at time $=T_d$ (45 h) for HCC70 cells treated with 0.1 μM AZD8055 and/or 0.32 μM rabusertib. Cells at S-phase entry and in early, mid-, and late S phase are gated (1–4).
(K) EdU content in S-phase cells in gates 2–4 in (J). ***$p < 0.001$ by Mann-Whitney U test; n.s.: not significant.
See also Figure S6.

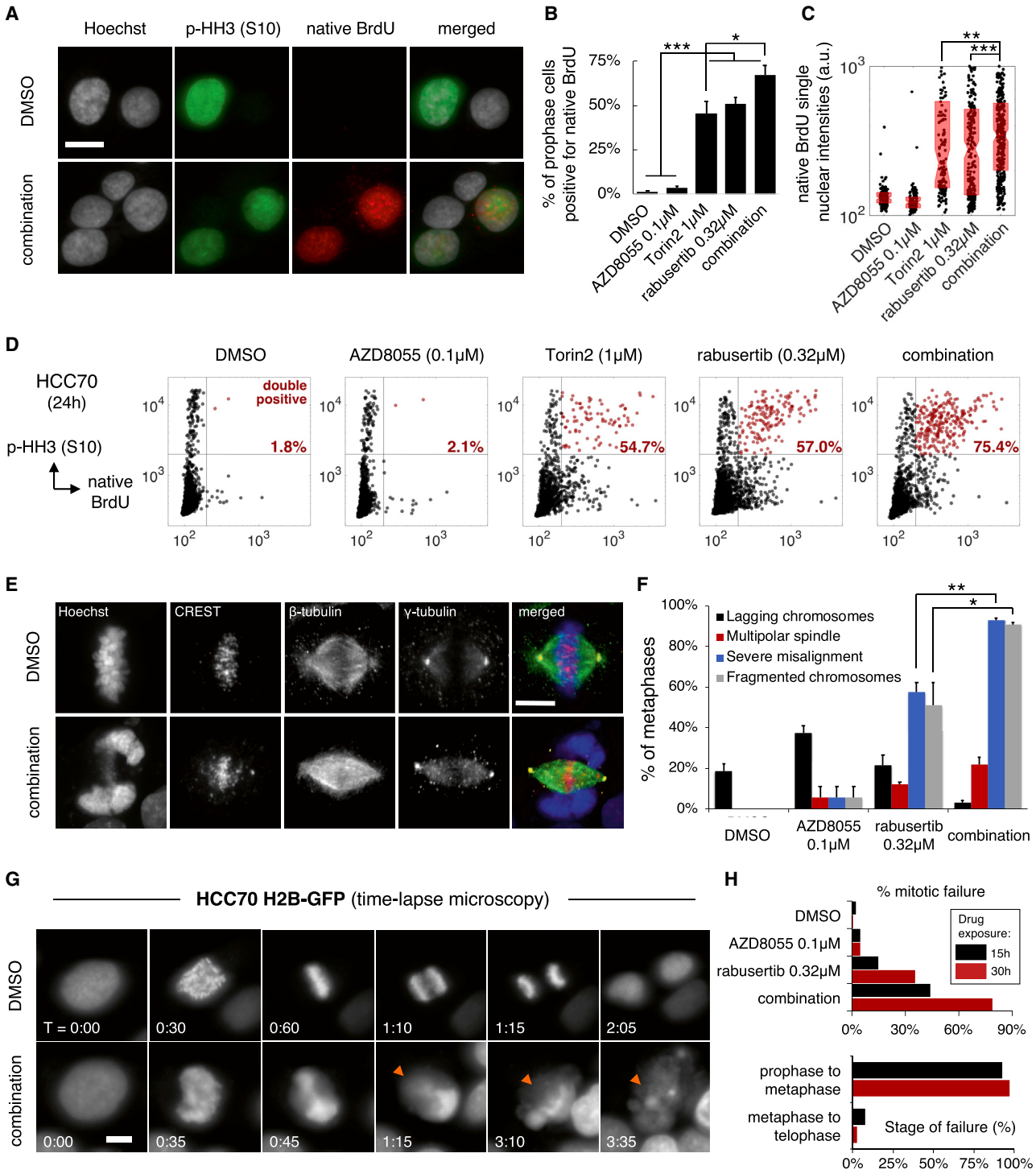

Figure 7. Low Doses of an mTOR Inhibitor and a Chk1 Inhibitor in Combination Cause Increased ssDNA in Mitotic Prophase and Death

"Combination" indicates 0.1 μM AZD8055 and 0.32 μM rabusertib. Data in (A)–(F) are from HCC70 cells after t = 0.5 × T_d (24 h) of drug exposure.

(A) Representative images of nuclei stained for Hoechst, p-HH3, and native BrdU; scale bar, 20 μM.

(B) Mean percent ± SEM of native BrdU and p-HH3 double-positive cells; n = 3 experiments.

(C) Native BrdU levels in single nuclei; boxplots show the median and 25th to 75th percentiles.

(D) Representative scatterplots quantifying p-HH3 and native BrdU double-positive cells (red); percentages are of p-HH3-positive (prophase) cells.

(E) Maximum intensity projections of confocal image stacks of metaphase cells; scale bar, 10 μm.

(F) Mean percent ± SEM of metaphases with the indicated aberrations; n = 2 experiments, 188 metaphases.

(legend continued on next page)

SUPPLEMENTAL INFORMATION

Supplemental Information can be found online at https://doi.org/10.1016/j.cels.2019.11.001.

ACKNOWLEDGMENTS

This work was funded by NIH/NCI grants HL127365 (to P.K.S. and N.S.G.) and CA225088 (to P.K.S. and S.S.C.), the DFCI Leadership Council (S.S.C.), Conquer Cancer Foundation of ASCO (S.S.C.), and NIH T32 CA9172-4 (S.S.C.). Mass spectrometry was supported in part by NIH grants CA120964 (J.M.A.) and CA006516 (J.M.A.). We thank U. Matulonis for her support and M. Hafner, J. Reyes, M. Yuan, and A. Chen for their assistance with experiments, analysis, and preparation of the manuscript.

AUTHOR CONTRIBUTIONS

S.S.C. led the study; S.S.C., A.J., M.C., and C.M. performed the experiments; S.S.C. analyzed the data; A.P. generated the models and isobolograms; J.M.A., M.N., C.Y., and J.-Y.C. contributed to the experimental design; Q.L. and S.C.S. assisted with the chemistry and N.S.G. and P.K.S. supervised the research. All authors have reviewed and approved the entire content of this submission.

DECLARATION OF INTERESTS

P.K.S. is a member of the SAB or Board of Directors of Merrimack Pharmaceuticals, Glencoe Software, Applied Biomath, and RareCyte and has equity in these companies. In the last five years, the Sorger lab has received research funding from Novartis and Merck. P.K.S. declares that none of these relationships are directly or indirectly related to the content of this manuscript. N.S.G. and Q.L. are co-inventors of Torin2, which is protected by the patent "Modulators of mTOR Complexes," European Patent Office EP2350053B1.

Received: October 11, 2018
Revised: July 11, 2019
Accepted: November 4, 2019
Published: December 4, 2019

REFERENCES

André, F., Ciruelos, E., Rubovszky, G., Campone, M., Loibl, S., Rugo, H.S., Iwata, H., Conte, P., Mayer, I.A., Kaufman, B., et al. (2019). Alpelisib for PIK3CA-mutated, hormone receptor-positive advanced breast cancer. N. Engl. J. Med. *380*, 1929–1940.

Ben-Sahra, I., Howell, J.J., Asara, J.M., and Manning, B.D. (2013). Stimulation of de novo pyrimidine synthesis by growth signaling through mTOR and S6K1. Science *339*, 1323–1328.

Ben-Sahra, I., Hoxhaj, G., Ricoult, S.J.H., Asara, J.M., and Manning, B.D. (2016). mTORC1 induces purine synthesis through control of the mitochondrial tetrahydrofolate cycle. Science *351*, 728–733.

Beronja, S., Livshits, G., Williams, S., and Fuchs, E. (2010). Rapid functional dissection of genetic networks via tissue-specific transduction and RNAi in mouse embryos. Nat. Med. *16*, 821–827.

Buisson, R., Boisvert, J.L., Benes, C.H., and Zou, L. (2015). Distinct but concerted roles of ATR, DNA-PK, and Chk1 in countering replication stress during S phase. Mol. Cell *59*, 1011–1024.

Cancer Genome Atlas Network. (2012). Comprehensive molecular portraits of human breast tumours. Nature *490*, 61–70.

Chia, S., Gandhi, S., Joy, A.A., Edwards, S., Gorr, M., Hopkins, S., Kondejewski, J., Ayoub, J.P., Califaretti, N., Rayson, D., and Dent, S.F. (2015). Novel agents and associated toxicities of inhibitors of the pi3k/Akt/mtor pathway for the treatment of breast cancer. Curr. Oncol. *22*, 33–48.

Costa, C., Ebi, H., Martini, M., Beausoleil, S.A., Faber, A.C., Jakubik, C.T., Huang, A., Wang, Y., Nishtala, M., Hall, B., et al. (2015). Measurement of PIP3 levels reveals an unexpected role for p110β in early adaptive responses to p110α-specific inhibitors in luminal breast cancer. Cancer Cell *27*, 97–108.

de Feraudy, S., Revet, I., Bezrookove, V., Feeney, L., and Cleaver, J.E. (2010). A minority of foci or pan-nuclear apoptotic staining of gammaH2AX in the S phase after UV damage contain DNA double-strand breaks. Proc. Natl. Acad. Sci. USA *107*, 6870–6875.

Duronio, R.J., and Xiong, Y. (2013). Signaling pathways that control cell proliferation. Cold Spring Harb. Perspect. Biol. *5*, a008904.

Elkabets, M., Vora, S., Juric, D., Morse, N., Mino-Kenudson, M., Muranen, T., Tao, J., Campos, A.B., Rodon, J., Ibrahim, Y.H., et al. (2013). mTORC1 inhibition is required for sensitivity to PI3K p110α inhibitors in PIK3CA-mutant breast cancer. Sci. Transl. Med. *5*, 196ra99.

Foulkes, W.D., Smith, I.E., and Reis-Filho, J.S. (2010). Triple-negative breast cancer. N. Engl. J. Med. *363*, 1938–1948.

Hafner, M., Niepel, M., Chung, M., and Sorger, P.K. (2016). Growth rate inhibition metrics correct for confounders in measuring sensitivity to cancer drugs. Nat. Methods *13*, 521–527.

Janku, F., Yap, T.A., and Meric-Bernstam, F. (2018). Targeting the PI3K pathway in cancer: are we making headway? Nat. Rev. Clin. Oncol. *15*, 273–291.

Johnson, K.R., Young, K.K., and Fan, W. (1999). Antagonistic interplay between antimitotic and G1-S arresting agents observed in experimental combination therapy. Clin. Cancer Res. *5*, 2559–2565.

Juvekar, A., Hu, H., Yadegarynia, S., Lyssiotis, C.A., Ullas, S., Lien, E.C., Bellinger, G., Son, J., Hok, R.C., Seth, P., et al. (2016). Phosphoinositide 3-kinase inhibitors induce DNA damage through nucleoside depletion. Proc. Natl. Acad. Sci. USA *113*, E4338–E4347.

King, C., Diaz, H.B., McNeely, S., Barnard, D., Dempsey, J., Blosser, W., Beckmann, R., Barda, D., and Marshall, M.S. (2015). LY2606368 causes replication catastrophe and antitumor effects through CHK1-dependent mechanisms. Mol. Cancer Ther. *14*, 2004–2013.

Knight, Z.A., Lin, H., and Shokat, K.M. (2010). Targeting the cancer kinome through polypharmacology. Nat. Rev. Cancer *10*, 130–137.

Liang, J., and Slingerland, J.M. (2003). Multiple roles of the PI3K/PKB (Akt) pathway in cell cycle progression. Cell Cycle *2*, 339–345.

Lin, A.B., McNeely, S.C., and Beckmann, R.P. (2017). Achieving precision death with cell-cycle inhibitors that target DNA replication and repair. Clin. Cancer Res. *23*, 3232–3240.

Liu, Q., Chang, J.W., Wang, J., Kang, S.A., Thoreen, C.C., Markhard, A., Hur, W., Zhang, J., Sim, T., Sabatini, D.M., and Gray, N.S. (2010). Discovery of 1-(4-

(G) Time-lapse imaging of HCC70 H2B-GFP cells showing aberrant chromatin condensation in cells treated with the combination, followed by abnormal metaphase (arrowhead) and death. Numbers denote hours:minutes; scale bar, 10 μm.
(H) Percent of failed mitoses after 15 or 30 h of drug exposure (top) and stage of all failed mitoses (bottom). N ~200 cells at each timepoint. *$p < 0.05$, **$p < 0.01$, ***$p < 0.001$, and n.s. (not significant) by ANOVA and Tukey's test (B and F, selected comparisons shown) and Mann-Whitney U test (C).
See also Figure S7.

(4-propionylpiperazin-1-yl)-3-(trifluoromethyl)phenyl)-9-(quinolin-3-yl)benzo [h][1,6]naphthyridin-2(1H)-one as a highly potent, selective mammalian target of rapamycin (mTOR) inhibitor for the treatment of cancer. J. Med. Chem. *53*, 7146–7155.

Liu, Q., Xu, C., Kirubakaran, S., Zhang, X., Hur, W., Liu, Y., Kwiatkowski, N.P., Wang, J., Westover, K.D., Gao, P., et al. (2013). Characterization of Torin2, an ATP-competitive inhibitor of mTOR, ATM, and ATR. Cancer Res. *73*, 2574–2586.

Ma, C.X., Janetka, J.W., and Piwnica-Worms, H. (2011). Death by releasing the breaks: CHK1 inhibitors as cancer therapeutics. Trends Mol. Med. *17*, 88–96.

Macheret, M., and Halazonetis, T.D. (2018). Intragenic origins due to short G1 phases underlie oncogene-induced DNA replication stress. Nature *555*, 112–116.

Munster, P., Aggarwal, R., Hong, D., Schellens, J.H.M., van der Noll, R., Specht, J., Witteveen, P.O., Werner, T.L., Dees, E.C., Bergsland, E., et al. (2016). First-in-human phase I study of GSK2126458, an oral pan-class I phosphatidylinositol-3-kinase inhibitor, in patients with advanced solid tumor malignancies. Clin. Cancer Res. *22*, 1932–1939.

Neef, A.B., and Luedtke, N.W. (2011). Dynamic metabolic labeling of DNA in vivo with arabinosyl nucleosides. Proc. Natl. Acad. Sci. USA *108*, 20404–20409.

Neve, R.M., Chin, K., Fridlyand, J., Yeh, J., Baehner, F.L., Févr, T., Clark, L., Bayani, N., Coppe, J.-P., Tong, F., et al. (2006). A collection of breast cancer cell lines for the study of functionally distinct cancer subtypes. Cancer Cell *10*, 515–527.

Sakaue-Sawano, A., Kurokawa, H., Morimura, T., Hanyu, A., Hama, H., Osawa, H., Kashiwagi, S., Fukami, K., Miyata, T., Miyoshi, H., et al. (2008). Visualizing spatiotemporal dynamics of multicellular cell-cycle progression. Cell *132*, 487–498.

Sampattavanich, S., Steiert, B., Kramer, B.A., Gyori, B.M., Albeck, J.G., and Sorger, P.K. (2018). Encoding growth factor identity in the temporal dynamics of FOXO3 under the combinatorial control of ERK and AKT kinases. Cell Syst. *6*, 664–678.e9.

Schwartz, S., Wongvipat, J., Trigwell, C.B., Hancox, U., Carver, B.S., Rodrik-Outmezguine, V., Will, M., Yellen, P., de Stanchina, E., Baselga, J., et al. (2015). Feedback suppression of PI3Kα signaling in PTEN-mutated tumors is relieved by selective inhibition of PI3Kβ. Cancer Cell *27*, 109–122.

Shi, Z., Azuma, A., Sampath, D., Li, Y.X., Huang, P., and Plunkett, W. (2001). S-phase arrest by nucleoside analogues and abrogation of survival without cell cycle progression by 7-hydroxystaurosporine. Cancer Res. *61*, 1065–1072.

Silvera, D., Ernlund, A., Arju, R., Connolly, E., Volta, V., Wang, J., and Schneider, R.J. (2017). mTORC1 and -2 coordinate transcriptional and translational reprogramming in resistance to DNA damage and replicative stress in breast cancer cells. Mol. Cell. Biol. *37*, e00577–16.

Spencer, S.L., Cappell, S.D., Tsai, F.C., Overton, K.W., Wang, C.L., and Meyer, T. (2013). The proliferation-quiescence decision is controlled by a bifurcation in CDK2 activity at mitotic exit. Cell *155*, 369–383.

Sui, M., Dziadyk, J.M., Zhu, X., and Fan, W. (2004). Cell cycle-dependent antagonistic interactions between paclitaxel and gamma-radiation in combination therapy. Clin. Cancer Res. *10*, 4848–4857.

Tallarida, R.J. (2011). Quantitative methods for assessing drug synergism. Genes Cancer *2*, 1003–1008.

Toledo, L.I., Altmeyer, M., Rask, M.B., Lukas, C., Larsen, D.H., Povlsen, L.K., Bekker-Jensen, S., Mailand, N., Bartek, J., and Lukas, J. (2013). ATR prohibits replication catastrophe by preventing global exhaustion of RPA. Cell *155*, 1088–1103.

Toledo, L.I., Murga, M., Zur, R., Soria, R., Rodriguez, A., Martinez, S., Oyarzabal, J., Pastor, J., Bischoff, J.R., and Fernandez-Capetillo, O. (2011). A cell-based screen identifies ATR inhibitors with synthetic lethal properties for cancer-associated mutations. Nat. Struct. Mol. Biol. *18*, 721–727.

Wang, W., Fridman, A., Blackledge, W., Connelly, S., Wilson, I.A., Pilz, R.B., and Boss, G.R. (2009). The phosphatidylinositol 3-kinase/Akt cassette regulates purine nucleotide synthesis. J. Biol. Chem. *284*, 3521–3528.

Zeman, M.K., and Cimprich, K.A. (2014). Causes and consequences of replication stress. Nat. Cell Biol. *16*, 2–9.

STAR★METHODS

KEY RESOURCES TABLE

REAGENT or RESOURCE	SOURCE	IDENTIFIER
Antibodies		
Rabbit monoclonal anti-phospho-AKT (Ser473) (D9E)	Cell Signaling (CST)	Cat#4060; RRID: AB_2315049
Rabbit monoclonal anti-phospho-AKT (Thr308) (D25E6)	Cell Signaling (CST)	Cat#13038; RRID: AB_2629447
Rabbit monoclonal anti-PTEN (D4.3)	Cell Signaling (CST)	Cat#9188; RRID: AB_2253290
Rabbit monoclonal anti-INPP4B (EPR3108Y)	Epitomics	Cat#2512-1; RRID: AB_1267213
Rabbit monoclonal anti-phospho-Chk1 (Ser317) (D12H3)	Cell Signaling (CST)	Cat#12302; RRID: AB_2783865
Rabbit anti-phospho-Chk2 (Thr68)	Cell Signaling (CST)	Cat#2661; RRID: AB_331479
Rabbit monoclonal anti-phospho-4E-BP1 (Thr37/46) (236B4)	Cell Signaling (CST)	Cat#2855; RRID: AB_560835
Rabbit monoclonal anti-phospho-S6 Ribosomal Protein (Ser235/236) (D57.2.2E)	Cell Signaling (CST)	Cat#4858; RRID: AB_916156
Rabbit monoclonal anti-phospho-Histone H2A.X (Ser139) (20E3)	Cell Signaling (CST)	Cat#9718; RRID: AB_2118009
Rabbit monoclonal anti-phospho-Histone H3 (Ser10) (D2C8)	Cell Signaling (CST)	Cat#3377; RRID: AB_1549592
Mouse monoclonal anti-β-Tubulin (D3U1W)	Cell Signaling (CST)	Cat#86298; RRID: AB_2715541
Rabbit monoclonal anti-β-Tubulin (9F3)	Cell Signaling (CST)	Cat#2128; RRID: AB_823664
Mouse monoclonal anti-BrdU (Bu20a)	Cell Signaling (CST)	Cat#5292; RRID: AB_10548898
Rabbit monoclonal anti-phospho-GSK3β (Ser9) (D85E12)	Cell Signaling (CST)	Cat#5558; RRID: AB_10013750
Rabbit monoclonal anti-FoxO3a (75D8)	Cell Signaling (CST)	Cat#2497; RRID: AB_836876
Rabbit monoclonal anti-p27 Kip1 (D69C12)	Cell Signaling (CST)	Cat#3686; RRID: AB_2077850
Rabbit monocolonal anti-phospho-Rb (Ser807/811) (D20B12)	Cell Signaling (CST)	Cat#8516; RRID: AB_11178658
Rabbit monoclonal anti-Cyclin D1 (EPR2241)	Abcam	Cat#ab134175; RRID: AB_2750906
Rabbit monoclonal anti-Geminin (EPR14637)	Abcam	Cat#ab195047
Rabbit monoclonal anti-Cyclin A2 (EPR17351)	Abcam	Cat#ab181591
Rabbit polyclonal anti-phospho-RPA32 (Ser4/8)	Bethyl	Cat#A300-245A; RRID: AB_210547
Rabbit polyclonal anti-γ-Tubulin	Sigma	Cat#T5192; RRID: AB_261690
Human anti-centromere	ImmunoVision	Cat#HCT-0100; RRID: AB_2744669
Donkey anti-Rabbit IgG (H+L) Highly Cross-Adsorbed Secondary Antibody, Alexa Fluor 647	Invitrogen	Cat#A-31573; RRID: AB_2536183
Donkey anti-Mouse IgG (H+L) Highly Cross-Adsorbed Secondary Antibody, Alexa Fluor 647	Invitrogen	Cat#A-31571; RRID: AB_162542
Goat anti-Human IgG (H+L) Cross-Adsorbed Secondary Antibody, Alexa Fluor 647	Invitrogen	Cat#A-21445; RRID: AB_2535862
Donkey anti-Rabbit IgG (H+L) Highly Cross-Adsorbed Secondary Antibody, Alexa Fluor 488	Invitrogen	Cat#A-21206; RRID: AB_2535792
Goat anti-Mouse IgG (H+L) Cross-Adsorbed Secondary Antibody, Alexa Fluor 488	Invitrogen	Cat#A-11001; RRID: AB_2534069
Goat anti-Rabbit IgG (H+L) Cross-Adsorbed Secondary Antibody, Alexa Fluor 568	Invitrogen	Cat#A-11011; RRID: AB_143157
Sheep IgG (H&L) Antibody IRDye800CW Conjugated Pre-Adsorbed	Rockland	Cat#613-431-028; RRID: AB_220177

(*Continued on next page*)

Continued

REAGENT or RESOURCE	SOURCE	IDENTIFIER
Bacterial and Virus Strains		
LV-GFP (lentivirus)	Beronja et al., 2010	Addgene Plasmid #25999
CSII-pEF-H2B-mTurquoise (lentivirus)	Spencer et al., 2013	N/A
CSII-pEF-mVenus-hGeminin(1–110) (lentivirus)	Sakaue-Sawano et al., 2008	N/A
Biological Samples	N/A	N/A
Chemicals, Peptides, and Recombinant Proteins		
alpelisib	MedChem Express	HY-15244; CAS: 1217486-61-7
apitolisib	MedChem Express	HY-13246; CAS: 1032754-93-0
AS-605240	MedChem Express	HY-10109; CAS: 648450-29-7
AZ20	MedChem Express	HY-15557; CAS: 1233339-22-4
AZD6482	Haoyuan Chemexpress	HY-10344; CAS: 1173900-33-8
AZD8055	MedChem Express	HY-10422; CAS: 1009298-09-2
buparlisib	Haoyuan Chemexpress	HY-70063; CAS: 944396-07-0
BX-912	Haoyuan Chemexpress	HY-11005; CAS: 702674-56-4
dactolisib	Haoyuan Chemexpress	HY-50673; CAS: 915019-65-7
everolimus	Haoyuan Chemexpress	HY-10218; CAS: 159351-69-6
KIN001-244	Nathanael Gray Laboratory at Dana-Farber Cancer Institute	N/A
idelalisib	Haoyuan Chemexpress	HY-13026; CAS: 870281-82-6
MK-2206	MedChem Express	HY-10358; CAS: 1032350-13-2
omipalisib	MedChem Express	HY-10297; CAS: 1086062-66-9
pictilisib	MedChem Express	HY-50094; CAS: 957054-30-7
PI-103	Haoyuan Chemexpress	HY-10115; CAS: 371935-74-9
PIK-93	Haoyuan Chemexpress	HY-12046; CAS: 593960-11-3
pilaralisib	Haoyuan Chemexpress	HY-11105; CAS: 956958-53-5
rabusertib	MedChem Express	HY-14720; CAS: 911222-45-2
rapamycin	MedChem Express	HY-10219; CAS: 53123-88-9
TGX-221	Haoyuan Chemexpress	HY-10114; CAS: 663619-89-4
Torin1	Nathanael Gray Laboratory at Dana-Farber Cancer Institute	N/A
Torin2	MedChem Express	HY-13002; CAS: 1223001-51-1
Torin2 analogs	Nathanael Gray Laboratory at Dana-Farber Cancer Institute	N/A
trametinib	Haoyuan Chemexpress	HY-10999; CAS: 871700-17-3
WYE-132	Haoyuan Chemexpress	HY-10044; CAS: 1144068-46-1
ZSTK474	Haoyuan Chemexpress	HY-50847; CAS: 475110-96-4
Critical Commercial Assays		
Odyssey blocking buffer in PBS	Li-COR	927-40000
LIVE/DEAD Fixable Far Red Dead Cell Stain Kit	Invitrogen	L10120
Click-iT Plus EdU Alexa Fluor 488 Imaging Kit	Thermo Fisher Scientific	C10637
IncuCyte Caspase-3/7 Green Apoptosis Assay Reagent	Essen Bioscience	4440
Hoechst 33342 trihydrochloride trihydrate	Invitrogen	H3570
5-Bromo-2′-deoxyuridine (BrdU)	Sigma Aldrich	B9285
(2′*S*)-2′-Deoxy-2′-fluoro-5-ethynyluridine (F-ara-EdU)	Sigma Aldrich	T511293
Cellomics Whole Cell Stain (blue)	Thermo Scientific	8403502

(*Continued on next page*)

Continued

REAGENT or RESOURCE	SOURCE	IDENTIFIER
Deposited Data		
Evaluation of the sensitivities of six triple-negative breast cancer (TNBC) cell lines to 23 different PI3K/AKT/mTOR inhibitors or to a MEK inhibitor (trametinib). Dataset 1 of 2: GR values - Dataset (ID:20364)	This paper; Harvard Medical School LINCS database	HMS LINCS Database: 20364; https://lincs.hms.harvard.edu/db/datasets/20364/
Evaluation of the sensitivities of six triple-negative breast cancer (TNBC) cell lines to 23 different PI3K/AKT/mTOR inhibitors or to a MEK inhibitor (trametinib). Dataset 2 of 2: GR metrics - Dataset (ID:20365)	This paper; Harvard Medical School LINCS database	HMS LINCS Database: 20365; https://lincs.hms.harvard.edu/db/datasets/20365/
Evaluation of the sensitivity of two triple-negative breast cancer cell lines (HCC1806, HCC70) to a collection of dual mTOR and PI3K-like kinase (PIKK) inhibitors. Dataset 1 of 2: GR values - Dataset (ID:20366)	This paper; Harvard Medical School LINCS database	HMS LINCS Database: 20366; https://lincs.hms.harvard.edu/db/datasets/20366/
Evaluation of the sensitivity of two triple-negative breast cancer cell lines (HCC1806, HCC70) to a collection of dual mTOR and PI3K-like kinase (PIKK) inhibitors. Dataset 2 of 2: GR metrics - Dataset (ID:20367)	This paper; Harvard Medical School LINCS database	HMS LINCS Database: 20367; https://lincs.hms.harvard.edu/db/datasets/20367/
Targeted metabolomics profiling data (i.e., peak intensity measurements) after acute exposure of BT-549 cells to DMSO or rapamycin, AZD8055 or Torin2 at two doses (100nM, 1000nM) for 6 hours - Dataset (ID:20368)	This paper; Harvard Medical School LINCS database	HMS LINCS Database: 20368; https://lincs.hms.harvard.edu/db/datasets/20368/
Breast Cancer Profiling Project, Drug Sensitivity phase I: Fixed-cell GR measures of 35 breast cell lines to 34 small molecule perturbagens from library plate I. Dataset 1 of 2: Normalized growth rate inhibition values - Dataset (ID:20343)	Harvard Medical School LINCS database	HMS LINCS Database: 20343; http://lincs.hms.harvard.edu/db/datasets/20343/
Breast Cancer Profiling Project, Drug Sensitivity phase I: Fixed-cell GR measures of 35 breast cell lines to 34 small molecule perturbagens from library plate I. Dataset 2 of 2: Calculated dose response metrics - Dataset (ID:20344)	Harvard Medical School LINCS database	HMS LINCS Database: 20344; http://lincs.hms.harvard.edu/db/datasets/20344/
Experimental Models: Cell Lines		
Human: HCC1806	ATCC	CRL-2335
Human: HCC70	ATCC	CRL-2315
Human: HCC38	ATCC	CRL-2314
Human: BT-20	ATCC	HTB-19
Human: BT-549	ATCC	HTB-122
Human: Hs 578T	ATCC	HTB-126
Human: HCC70 H2B-GFP	This paper	N/A
Human: HCC1806 H2B-mTurquoise, mVenus-hGeminin(1-110)	This paper	N/A
Human: Hs 578T NLS-mCherry	Sampattavanich, et al., 2018	N/A
Human: HCC1806 NLS-mCherry	Sampattavanich, et al., 2018	N/A
Software and Algorithms		
Columbus Image Data Storage and Analysis Software	Perkin Elmer	http://www.perkinelmer.com/product/image-data-storage-and-analysis-system-columbus
Incucyte Zoom Software	Essen Bioscience	https://www.essenbioscience.com/en/products/software/incucyte-base-software/

(*Continued on next page*)

Continued

REAGENT or RESOURCE	SOURCE	IDENTIFIER
MATLAB	MathWorks	N/A
Metaboanalyst 4.0		https://www.metaboanalyst.ca/
Mathematica	Wolfram	N/A
GR Calculator	HMS LINCS Center	http://www.grcalculator.org/grcalculator/
Other		
Operetta High-Content Imaging System	Perkin Elmer	HH12000000
Incucyte Zoom	Essen Bioscience	N/A
In Cell Analyzer 6000	GE Healthcare Life Sciences	N/A
ImageXpress Micro Confocal High-Content Imaging System	Molecular Devices	N/A
EL406 Washer Dispenser	BioTek	N/A
Cell Carrier 384 well plates for imaging	Perkin Elmer	6007550
Odyssey Imager	Li-COR Biosciences	N/A
D300 Digital Dispenser	Hewlett Packard	N/A

LEAD CONTACT AND MATERIALS AVAILABILITY

Further information and requests for resources and reagents should be directed to and will be fulfilled by the Lead Contact, Peter Sorger (peter_sorger@hms.harvard.edu).

Materials Availability Statement

All unique/stable reagents generated in this study are available from the Lead Contact with a completed Materials Transfer Agreement.

EXPERIMENTAL MODEL AND SUBJECT DETAILS

Cell Lines

The media and culture conditions for all breast cancer and non-transformed mammary epithelial cell lines used in this study are described below. All cell lines were isolated from females, to the best of our knowledge. STR profiling was performed to confirm cell line identity.

Cell line	RRID	Growth medium (FBS: heat-inactivated fetal bovine serum; P/S: penicillin/streptomycin)	Temp	CO_2
184-B5	CVCL_4688	MEBM (Lonza/Clonetics; MEGM Kit #CC-3150) + 1ng/ml cholera toxin (unfiltered)	37°C	5%
AU-565	CVCL_1074	RPMI-1640 + 10% FBS + 1% P/S	37°C	5%
BT-20	CVCL_0178	EMEM + 10% FBS + 1% P/S	37°C	5%
BT-474	CVCL_0179	RPMI-1640 + 10% FBS + 1% P/S	37°C	5%
BT-483	CVCL_2319	RPMI-1640 + 20% FBS + 1% P/S + 0.01mg/ml bovine insulin	37°C	5%
BT-549	CVCL_1092	RPMI-1640 + 10% FBS + 1% P/S + 0.023IU/ml insulin	37°C	5%
CAL-120	CVCL_1104	DMEM + 10% FBS + 1% P/S	37°C	5%
CAL-51	CVCL_1110	DMEM + 20% FBS + 1% P/S	37°C	5%
CAL-85-1	CVCL_1114	DMEM + 10% FBS + 1% P/S	37°C	5%
CAMA-1	CVCL_1115	EMEM + 10% FBS + 1% P/S	37°C	5%
HCC1143	CVCL_1245	RPMI-1640 + 10% FBS + 1% P/S	37°C	5%
HCC1395	CVCL_1249	RPMI-1640 + 10% FBS + 1% P/S	37°C	5%
HCC1419	CVCL_1251	RPMI-1640 + 10% FBS + 1% P/S	37°C	5%

(*Continued on next page*)

Continued

Cell line	RRID	Growth medium (FBS: heat-inactivated fetal bovine serum; P/S: penicillin/streptomycin)	Temp	CO_2
HCC1428	CVCL_1252	RPMI-1640 + 10% FBS + 1% P/S	37°C	5%
HCC1500	CVCL_1254	RPMI-1640 + 10% FBS + 1% P/S	37°C	5%
HCC1569	CVCL_1255	RPMI-1640 + 10% FBS + 1% P/S	37°C	5%
HCC1806	CVCL_1258	RPMI-1640 + 10% FBS + 1% P/S	37°C	5%
HCC1937	CVCL_0290	RPMI-1640 + 10% FBS + 1% P/S	37°C	5%
HCC1954	CVCL_1259	RPMI-1640 + 10% FBS + 1% P/S	37°C	5%
HCC202	CVCL_2062	RPMI-1640 + 10% FBS + 1% P/S	37°C	5%
HCC38	CVCL_1267	RPMI-1640 + 10% FBS + 1% P/S	37°C	5%
HCC70	CVCL_1270	RPMI-1640 + 10% FBS + 1% P/S	37°C	5%
Hs 578T	CVCL_0332	DMEM + 10% FBS + 1% P/S	37°C	5%
hTERT-HME1	CVCL_3383	MEBM + Lonza CC-3150 kit	37°C	5%
MCF-10A	CVCL_0598	1:1 DMEM and Ham's F12 + 20 ng/ml human epidermal growth factor + 100 ng/ml cholera toxin + 0.01 mg/ml bovine insulin + 500 ng/ml hydrocortisone, 95% + 5% horse serum	37°C	5%
MCF-10F	CVCL_3633	1:1 DMEM and Ham's F12 + 20 ng/ml human epidermal growth factor + 100 ng/ml cholera toxin + 0.01 mg/ml bovine insulin + 500 ng/ml hydrocortisone, 95% + 5% horse serum	37°C	5%
MCF-12A	CVCL_3744	1:1 DMEM and Ham's F12 + 20 ng/ml human epidermal growth factor + 100 ng/ml cholera toxin + 0.01 mg/ml bovine insulin + 500 ng/ml hydrocortisone, 95% + 5% horse serum	37°C	5%
MCF-7	CVCL_0031	DMEM + 10% FBS + 1% P/S	37°C	5%
MDA-MB-134-VI	CVCL_0617	Leibovitz's L-15 + 20% FBS (not heat-inactivated) + 1% P/S	37°C	0%
MDA-MB-157	CVCL_0618	Leibovitz's L-15 +10% FBS (not heat-inactivated) + 1% P/S	37°C	0%
MDA-MB-175-VII	CVCL_1400	Leibovitz's L-15 +10% FBS (not heat-inactivated) + 1% P/S	37°C	0%
MDA-MB-231	CVCL_0062	DMEM (or L-15) + 10% FBS (not heat-inactivated) + 1% P/S	37°C	0%
MDA-MB-361	CVCL_0620	Leibovitz's L-15 + 20% FBS (not heat-inactivated) + 1% P/S	37°C	0%
MDA-MB-415	CVCL_0621	Leibovitz's L-15 + 15% FBS (not heat-inactivated) + 1% P/S + 2mM L-glutamine + 10mg/l insulin	37°C	0%
MDA-MB-436	CVCL_0623	Leibovitz's L-15 + 10% FBS (not heat-inactivated) + 1% P/S + 10mg/l insulin	37°C	0%
MDA-MB-453	CVCL_0418	Leibovitz's L-15 + 10% FBS (not heat-inactivated) + 1% P/S	37°C	0%
MDA-MB-468	CVCL_0419	Leibovitz's L-15 + 10% FBS (not heat-inactivated) + 1% P/S	37°C	0%
SK-BR-3	CVCL_0033	McCoy's 5a + 10% FBS + 1% P/S	37°C	0%
SUM102PT	CVCL_3421	Ham's F-12 + 1% P/S + 5 μg/ml insulin + 1μg/ml hydrocortisone + 10 ng/mL epidermal growth factor + 5 mM ethanolamine + 10 mM HEPES + 5 μg/mL transferrin + 10 nM T3 + 50nM sodium selenite + 1 g/L BSA	37°C	5%
SUM1315MO2	CVCL_5589	Ham's F-12 + 5% FBS + 1% P/S + 10 ng/ml human epidermal growth factor + 5 μg/ml insulin + 10 mM HEPES	37°C	5%

(*Continued on next page*)

Continued

Cell line	RRID	Growth medium (FBS: heat-inactivated fetal bovine serum; P/S: penicillin/streptomycin)	Temp	CO_2
SUM149PT	CVCL_3422	Ham's F-12 + 5% FBS + 1% P/S + 1 μg/ml hydrocortisone + 5 μg/ml insulin + 10 mM HEPES	37°C	5%
SUM159PT	CVCL_5423	Ham's F-12 + 5% FBS + 1% P/S + 1 ng/ml hydrocortisone + 5 μg/ml insulin + 10 mM HEPES	37°C	5%
SUM225CWN	CVCL_5593	Ham's F-12 + 5% FBS + 1% P/S + 5 μg/ml insulin + 1 μg/ml hydrocortisone + 10 mM HEPES	37°C	5%
SUM44PE	CVCL_3424	Ham's F-12 + 1% P/S + 5 μg/ml insulin + 1 μg/ml hydrocortisone + 5 mM ethanolamine + 10 mM HEPES + 5 μg/mL transferrin + 10 nM T3 + 50 nM sodium selenite + 1 g/L BSA	37°C	5%
SUM52PE	CVCL_3425	Ham's F-12 + 5% FBS + 1% P/S + 5 μg/ml insulin + 1 μg/ml hydrocortisone + 10 mM HEPES	37°C	5%
T-47D	CVCL_0553	RPMI-1640 + 10% FBS + 1% P/S + 0.2 units/ml bovine insulin	37°C	5%
UACC-812	CVCL_1781	Leibovitz's L-15 + 20% FBS (not heat-inactivated) + 1% P/S + 2 mM L-glutamine + 20 ng/ml human EGF	37°C	0%
UACC-893	CVCL_1782	Leibovitz's L-15 + 10% FBS (not heat-inactivated) + 1% P/S	37°C	0%
ZR-75-1	CVCL_0588	RPMI-1640 + 10% FBS + 1% P/S	37°C	5%
ZR-75-30	CVCL_1661	RPMI-1640 + 10% FBS + 1% P/S	37°C	5%

Cell Line Generation

HCC70 H2B-GFP cells were established via lentiviral transduction (Addgene, 25999) followed by fluorescence-activated cell sorting (FACS) sorting for GFP-positive cells (Beronja et al., 2010). HCC1806 cells expressing H2B-mTurquoise and mVenus-hGeminin (1–110) were established via sequential lentiviral transduction of CSII-pEF-H2B-mTurquoise and CSII-pEF-mVenus-geminin (1–110), followed by (FACS) for mTurquoise and mVenus double-positive cells (Sakaue-Sawano et al., 2008; Spencer et al., 2013). The generation of Hs 578T NLS-mCherry and HCC1806 NLS-mCherry cell lines, which also express a F3aN400-Venus construct not utilized here, was previously described (Sampattavanich et al., 2018). The media and culture conditions for genetically-engineered cell lines were identical to the parental cell lines.

METHOD DETAILS

Western Blotting

To determine protein levels under unstimulated conditions, cells grown to approximately 75% confluency under the conditions described above were serum starved overnight and then lysed with Mammalian Protein Extraction buffer (M-PER; Thermo Scientific, 78501) supplemented with protease inhibitor cocktail (Sigma-Aldrich, P2714), 1mM sodium orthovanadate (Sigma-Aldrich, S6508), 5mM sodium pyrophosphate (Sigma-Aldrich, 221368), 50μM oxophenylarsine (EMD Biosciences, 521000) and 10mM bpV (phen) (EMD Biosciences, 203695). Two independent protein lysates were prepared from SK-BR-3 cells, and MDA-MB-231 cells were cultured in two different types of media (=total 48 samples for 46 different cell lines). Lysed cells were scraped off the plate, collected in microcentrifuge tubes and incubated on ice for 30min. Membranes and cell debris were sedimented by centrifugation at 20,000xg for 10min at 4°C. Supernatants were pooled, aliquoted and stored at −80°C. Protein concentration was determined using the Pierce BCA protein assay kit (Thermo Fisher Scientific, 23225). Protein electrophoresis was performed using E-PAGE pre-cast 8% gels with 48 wells (Thermo Fisher Scientific, EP04808). Separated protein was transferred to Immobilon-FL PVDF membranes (EMD Millipore, IPFL00005) using the Criterion blotting system (Bio-Rad). Membranes were blocked for 1 h at room temperature (RT) with Odyssey blocking buffer (OBB; Li-COR 927–40000), incubated in primary antibodies in OBB overnight at 4°C, washed for 30min in PBS plus 0.1% Tween-20 (PBST), incubated in secondary antibody in OBB for 1 h at RT, and washed again for 30min in PBST. Anti-PTEN (Cell Signaling Technologies, 9188) and anti-INPP4B (Epitomics, 2512–1) primary antibodies were each used at 1:1000 dilution. Detection was performed using anti-rabbit IRDye 800CW pre-adsorbed secondary antibody (Rockland, 613-431-028) at 1:20,000 dilution. The fluorescence intensity of bands was quantified using the Odyssey system (Li-COR).

Evaluation of Drug Sensitivity

All compounds except Torin2 analogs were obtained from MedChem Express. Stock solutions were prepared at a concentration of 10mM in DMSO and stored at -30°C. Torin2 analogs (QL-VIII-58, QL-V-107, QL-IV-100, QL-VI-86, QL-XII-47, QL-V-73, QL-X-138, QL-XII-108, QL-XII-61) were obtained from the laboratory of Nathanael Gray (Dana-Farber Cancer Institute) as 10mM stock solutions in DMSO. PI3K pathway drugs were arrayed in master library plates and pin-transferred to cells in Cell Carrier 384 well plates (PerkinElmer, 6007550). Torin2 analogs were delivered to cells in Cell Carrier 384 well plates using the D300 digital dispenser and accompanying software (Hewlett Packard). Cells were plated at a density of 1,000-2,000 cells per well using the Multidrop Combi (Thermo Scientific) and treatments were performed on the following day approximately 18-24h after plating. Inhibitors were administered at 9 different concentrations in at least technical triplicate and DMSO alone was used as a control. To determine cell number at the start (time = 0) and end (t = 72h) of treatment, cells were arrayed in two different plates with the time = 0 plate receiving no treatment and the 72h plate receiving DMSO control and active drug. Viable cells were identified using 15μL of staining solution, comprising 1:5,000 LIVE/DEAD Far Red Dead Cell Stain (Invitrogen, L10120), 1:10,000 Hoechst 33342 trihydrochloride trihydrate 10 mg/mL solution in water (Invitrogen, H3570) and 1:10 OptiPrep (Sigma-Aldrich, D1556) in PBS. Cells were incubated in staining solution for 30min at 37°C with 5% CO_2 and then fixed with 20μL fixing solution, comprising 1:20 37% formaldehyde (Sigma-Aldrich, F1635) and 1:5 OptiPrep in PBS, for 30min at RT. To achieve accurate cell counts, no aspiration of well contents was performed prior to fixing cells. Following fixation, all reagents were aspirated and replaced with 60μL of PBS using an EL406 Washer Dispenser (BioTek). Cells were imaged using the Operetta High-Content Imaging System (PerkinElmer). Six fields of view spanning each well in its entirety were acquired using the 10x high-NA objective lens and appropriate excitation/emission filters for Hoechst and LIVE/DEAD Far Red cell stains. The total viable cell count per well was determined using Columbus image analysis software (PerkinElmer), as described below.

Drug Dosing

When possible, GR_{max} doses of drugs were used to facilitate a principled comparison of drug activities. However, for certain experiments, decreased drug doses were used due to excessive cell death or growth inhibition that resulted in insufficient cells for analysis (e.g. DNA synthesis in surviving cell fractions; EdU content in post-treatment S-phase fractions, etc.). For the F-ara-EdU data presented in Figure 1E, Torin2 and omipalisib were used at 0.3xGR_{max} (1μM). For the signaling data presented in Figure 2A, Torin2 and omipalisib were used at 0.3xGR_{max} (1μM) in HCC1806 cells. For the cell cycle data presented in Figure 2C, Torin2 and omipalisib were used at 0.3xGR_{max} dose (BT-20: 1μM; HCC70: 0.32–1μM; HCC1806: 1μM). For the scatterplot data from HCC70 cells appearing in the middle and bottom rows of panels in Figure 2D, Torin2 and omipalisib were used at 0.1xGR_{max} dose (0.1–0.32μM). For the analysis of EdU content presented in Figure 2E, drug doses for HCC70 and HCC1806 cells were as described for Figure 2C. For Hs 578T cells, Torin2 and omipalisib were used at 0.3xGR_{max} dose (1μM). For BT-549 cells, AZD8055 was used at 0.3xGR_{max} dose (0.32μM) and omipalisib and Torin2 were used at 0.03xGR_{max} dose (0.1μM). For metabolomics profiling data presented in Figure 2F, GR_{max} doses of rapamycin and AZD8055 were used (1μM) and compared to a 0.3xGR_{max} dose of Torin2 (also 1μM).

Immunofluorescence Microscopy

Cells were plated in Cell Carrier 384 well plates at either 1,000 (Hs 578T) or 2,000 (BT-20, BT-549, HCC1806, HCC38, HCC70) cells per well, treated with active drug or DMSO using the D300 digital dispenser, and fixed at various timepoints using 4% formaldehyde in PBS for 30min at RT. Cells were washed twice with PBS for 5min each at RT using the EL406 automated plate washer, permeabilized with 0.25% Triton X-100 (Bio-Rad, 1610407) in PBS for 15min, washed twice again for 5min each with PBS and blocked with OBB for at least 1h at RT. Cells were incubated with primary antibody diluted in OBB overnight at 4°C. The following morning, cells were washed three times with PBST for 5min each and then stained with secondary antibodies diluted 1:2,000 in OBB for 1h at RT. Secondary antibodies varied for different experiments but included Alexa Fluor 647 donkey anti-rabbit (Invitrogen, A31573), Alexa Fluor 647 donkey anti-mouse (Invitrogen, A31571), Alexa Fluor 647 goat anti-human (Invitrogen, A21445), Alexa Fluor 488 donkey anti-rabbit (Invitrogen, A21206), Alexa Fluor 488 goat anti-mouse (Invitrogen, A11001), and Alexa Fluor 568 goat anti-rabbit (Invitrogen, A11011). Cells were washed twice with PBST and once with PBS for 5min each prior to staining with Hoechst 33342 (Thermo Scientific, 1:10,000 in PBS) for 30min at RT. To facilitate segmentation of signal intensities specifically in the nucleus, cytoplasm, or whole cell in certain experiments, cells were simultaneously stained with 1:5000 Cellomics Whole Cell Stain (Thermo Scientific, 8403502) in PBS. Cells were washed twice with PBS, sealed with foil, and imaged using the Operetta High-Content Imaging System, the ImageXpress Micro Confocal High-Content Imaging System (Molecular Devices) or the IN Cell Analyzer 6000 (GE Healthcare Life Sciences) using the appropriate excitation and emission filters, depending on the specific assay.

Primary Antibodies and Dilutions

The following primary antibodies were obtained from Cell Signaling Technology (catalog number, dilution in OBB): rabbit anti-phospho-AKT T308 (13038, 1:400), rabbit anti-phospho-AKT S473 (4060, 1:200), rabbit anti-phospho-Chk1 S317 (12302, 1:800), rabbit anti-phospho-Chk2 T68 (2661, 1:100), rabbit anti-phospho-4E-BP1 T37/46 (2855, 1:200), rabbit anti-phospho-S6 S235/236 (4858, 1:1000), rabbit anti-phospho-H2A.X S139 ("γH2A.X") (9718, 1:400), rabbit anti-phospho-histone H3 S10 (3377, 1:800), mouse anti-β-tubulin (86298, 1:400), rabbit anti-β-tubulin (2128, 1:400), mouse anti-BrdU (Bu20a) (5292, 1:200), rabbit anti-phospho-GSK3B S9 (5558, 1:400), rabbit anti-FOXO3 (2497, 1:200), rabbit anti-p21 (2947, 1:400), rabbit anti-p27 (3686, 1:400), and rabbit anti-phospho-Rb S807/811

(8516, 1:800). The following primary antibodies were obtained from Abcam (catalog number, dilution in OBB): rabbit anti-cyclin D1 (ab134175, 1:100), rabbit anti-geminin (ab195047, 1:100), and rabbit anti-cyclin A2 (ab181591, 1:500). Rabbit anti-phospho-RPA S4/8 antibodies were obtained from Bethyl (A300-245A, 1:400), rabbit anti-γ-tubulin antibodies from Sigma (T5192, 1:400), and Human antibody against Centromere (CREST) antibodies from ImmunoVision (HCT-0100, 1:1000).

Single-Stranded DNA (ssDNA) and Cell-Cycle Analysis

To measure ssDNA, newly-synthesized DNA in proliferating cells was first labeled with 10μM BrdU (Sigma, B9285) in growth media for a time equal to the measured cell line division time (T_d) in culture. Drug treatments were administered to labeled cells at T_d using the D300 digital dispenser, and cells were fixed at various timepoints using 4% formaldehyde. BrdU was detected under non-denaturing ("native") conditions by standard immunofluorescence microscopy, as described above. Cell-cycle analysis was performed after treating cells with active drug or DMSO-only control for time=T_d, which was 28h for HCC1806 cells, 32h for Hs 578T cells, 40h for BT-549 cells, 45h for both HCC70 and HCC38 cells and 48h for BT-20 cells. Active S-phase cells were labeled with 10μM EdU (Thermo Fisher Scientific, C10637) in growth media for 0.025xT_d in an incubator. Cells were then fixed with 4% formaldehyde in PBS for 30min at RT. Incorporated EdU was detected using the Click-iT EdU Plus Alexa Fluor 488 imaging kit (Thermo Fisher Scientific, C10637), per the manufacturer's instructions. Following the Click-iT reaction, cells were counterstained with 5μg/mL Hoechst dye and imaged using the Operetta or ImageXpress Micro Confocal High-Content Imaging System. In certain experiments, EdU-labeled cells were counterstained with anti-geminin, anti-cyclin A2, anti-phospho-pRb or anti-phospho-H2A.X antibodies overnight following the Click-iT reaction and prior to Hoechst staining. Continuous labeling of S-phase cells was performed using 1μM F-ara-EdU (Sigma, T511293) for 48 or 75h.

Live-Cell Microscopy

Time-lapse imaging of proliferation and apoptosis in live cells was performed using the Incucyte Zoom live-cell analysis system (Essen Bioscience) inside of an incubator maintained at 37°C and 5% CO_2. Cells were plated at low density in 384-well plates (Corning, 3712) and images were taken of whole wells every 30–120min using the 4× lens. Drugs were administered during logarithmic-phase growth. For proliferation assays, stable cell lines with nuclear-expressing fluorophores (HCC70 H2B-GFP, Hs 578T NLS-mCherry, HCC1806 NLS-mCherry) were used to quantify live cell number at regular time intervals. Apoptotic cells were identified in wild-type cell lines using the Incucyte caspase-3/7 apoptosis assay reagent (Essen Bioscience, 4440), which was added to growth media at the recommended final concentration (5μM) several hours in advance of drug treatment. For each experimental replicate, the number of apoptotic cells was measured for each drug, dose, timepoint and cell line in technical triplicate.

For live-cell studies of mitosis, HCC70 H2B-GFP cells were plated at 2,000 cells per well in Cell Carrier 384-well plates. Plates were kept in a standard tissue culture incubator maintained at 37°C and 5% CO_2 for approximately 48h before cells were treated with drugs using the D300 digital dispenser. Starting at either 15 or 30h after drug treatment, cells were imaged every 5-10 minutes for 5-7h in a humidified chamber maintained at 37°C and 5% CO_2 using the 40x/0.95 NA lens of the IN Cell Analyzer 6000 microscope. The rate of mitotic entry and the percentage and stage of aberrations were visually scored for individual cells followed from prophase through cytokinesis in time-lapse image stacks.

To analyze the effects of drugs on cells in different stages of the cell cycle, HCC1806 cells expressing H2B-mTurquoise and mVenus-hGeminin(1-110) were plated at 4,000 cells per well in 96-well plates (Ibidi, 89626), kept in a standard tissue culture incubator overnight, treated with drugs the next morning using the D300 digital dispenser and then imaged every 12min for 48 h in a humidified chamber maintained at 37°C and 5% CO_2 using the 20x/0.75NA lens of the ImageXpress Micro high-content imaging system with binning 2x2. To minimize the effect of phototoxicity, cells were imaged at minimal laser intensity and exposure times necessary to achieve approximately 8-fold actual signal intensity versus background for each fluorophore. At the end of the experiment, cells were stained with Hoechst and LIVE/DEAD stain to identify and quantify viable cells. To assess for possible phototoxicity, cell counts for DMSO-only control wells on the same plate that did not undergo imaging were compared to cell counts for DMSO-only control wells that underwent time-lapse imaging. To validate environmental conditions such as temperature, humidity, and CO_2, viable cells in an identically-treated plate kept in a standard tissue culture incubator set at 37°C and 5% CO_2 for 48 h (i.e., the duration of the experiment) were also compared by Hoechst and LIVE/DEAD co-staining.

Extraction of Polar Metabolites

Measurement of intracellular polar metabolite levels was performed to detect drug-induced changes in metabolic activity including *de novo* nucleotide biosynthesis and salvage pathways. BT-549 cells were selected for profiling following short drug exposure (i.e., 6 h) because inhibition of DNA synthesis was observed in S-phase cells (i.e., decreased EdU incorporation) prior to any detectable changes in cell cycle distribution, which can strongly bias metabolite levels. Cells in complete media were plated in 10 cm^2 dishes at 2.5x10^6 cells per dish and cultured at 37°C and 5% CO_2. Approximately two days later when cells were 75-80% confluent, the media was replaced with 10mL of fresh media containing rapamycin, AZD8055 or Torin2, or an equivalent volume of DMSO. After 6h of treatment, the 10cm^2 dishes were placed on dry ice and the media was aspirated and replaced with ice cold 80% (v/v) methanol. Dishes were kept at -80°C for 20min prior to using a cell scraper to produce a cell lysate/methanol mixture. The mixture for each sample was collected in a 15mL Eppendorf tube and cellular debris and protein were pelleted by centrifugation at 1,800xg for 5min at 4°C. The methanol supernatant containing polar metabolites was transferred to a new 15mL tube on dry ice and the cell debris/protein pellets were resuspended two additional times with methanol, centrifuged and re-pelleted. Recovered methanol supernatants for

each sample were pooled and then divided equally into four 1.5mL tubes on dry ice. Methanol was evaporated using a SpeedVac (no applied heat) and the resulting polar metabolite pellets were stored at -80°C.

Metabolomics Profiling by Targeted Mass Spectrometry

Metabolites were resuspended in 20mL HPLC-grade water for mass spectrometry. 5-7μL were injected and analyzed using a hybrid 5500 QTrap triple quadrupole mass spectrometer (AB/Sciex) coupled to a Prominence UFPLC system (Shimadzu) via selected reaction monitoring (SRM) of a total of 262 endogenous water-soluble metabolites for steady-state analyses of samples. Some metabolites were targeted in both positive and negative ion mode for a total of 298 SRM transitions using positive/negative ion polarity switching. ESI voltage was +4950V in positive ion mode and –4500V in negative ion mode. The dwell time was 3msec per SRM transition, and the total cycle time was 1.55sec. Approximately 10-14 data points were acquired per detected metabolite. Samples were delivered to the mass spectrometer via hydrophilic interaction chromatography (HILIC) using a 4.6mm i.d. x 10-cm amide XBridge column (Waters) at 400 μL/min. Buffer A was comprised of 20-mM ammonium hydroxide/20-mM ammonium acetate (pH=9.0) in 95:5 water:acetonitrile and Buffer B was HPLC grade acetonitrile. Gradients were run starting from 85% buffer B (in buffer A) to 42% B from 0-5min; 42% B to 0% B from 5-16min; 0% B was held from 16-24min; 0% B to 85% B from 24-25min; 85% B was held for 7min to re-equilibrate the column. Peak areas from the total ion current for each metabolite SRM transition were integrated using MultiQuant v2.1 software (AB/Sciex).

Isobolograms and Analysis of Drug Interactions

Viable cell counts were determined after exposure to PI3K pathway and ATR or Chk1 inhibitors administered in combinations over two-dimensional gradients. Dose ranges typically spanned at least one order of magnitude and were selected based on the GR_{50} values for each single agent. Continuous interpolations were constructed over the 2D response surface, which were then plotted as contour maps that highlight contours of equal inhibitory effect, or isoboles (Interpolation function and ContourPlot functions in Mathematica v11). As described by the Loewe additivity model, drug combinations were classified as additive or better based on the concept of dose equivalence, which manifests as diagonal isoboles that intersect both axes. Combinations were classified as antagonistic when isoboles were observed to deviate away from either axis, indicating that the drugs used together were less effective than either drug used alone. Combinations were classified as having no interaction when the activity of each drug appeared to be unaffected by the second drug, indicating independent action and manifested by linear isoboles. Examples of each case are shown in Figure 6G.

Cell-Cycle Model and Simulation of Combinatorial Drug Effect

The effects of mTOR and ATR or Chk1 inhibition individually or in combination were simulated by a discrete time-step Monte Carlo simulation. This simulation followed the progress of individual cells through the G1, S, G2, and M phases of the cell cycle, with each cell possessing a cell-state variable that increments with cell cycle progression. When a cell completed M phase, the mother cell was replaced by two daughter cells at the start of G1. Simulations were initialized with a population of 300 cells distributed throughout the cell cycle (i.e., asynchronous) based on experimentally measured cell cycle distributions for TNBC. mTOR inhibition slowed each cell's progress through G1 (*independence* model) or through both G1 and S phases (*interaction* model) by imposing a lower probability per time-step that the cell-state variable will increase. ATR or Chk1 inhibition imposed on each S-phase cell a specific rate of lethal replication block at each time-step. In light of prior knowledge that the effects of ATR or Chk1 inhibition during replication can ultimately cause death of cells in S phase (replication catastrophe) or in mitosis (mitotic catastrophe), simulations did not discriminate between whether the moment of death arises in S phase or in mitosis. In the *interaction* model, slowing of cells through S phase by mTOR inhibition was found to elicit an increase in the accumulated probability of lethal damage caused by ATR or Chk1 inhibition.

QUANTIFICATION AND STATISTICAL ANALYSIS

Details regarding the number of experimental replicates, specific statistical tests used and the level of significance are described in the primary and supplementary figure legends. Significant differences are also indicated on the primary and supplemental figures.

Viable Cell Counts

Images of TNBC cells co-stained with Hoechst and LIVE/DEAD stains were analyzed using Columbus image data storage and analysis system (PerkinElmer) in order to quantify the total number of viable cells per well. Nuclear segmentation was performed using the Hoechst fluorescence intensity. For example, the number of HCC1806 cell nuclei in a particular well was determined using the following segmentation routine: module: 'Find Nuclei'; Channel: 'Hoechst'; Method: M; diameter 28μm; splitting coefficient: 0.45; common threshold: 0.05. Because of differences in nuclear size and morphology, optimal segmentation routines varied for each TNBC cell line and were determined in an empirical fashion. After identification of all nuclei in a well, additional features were extracted from images to exclude over/under segmented nuclei, doublets and non-viable cells from the total cell counts. Over/under segmented nuclei and doublets were of atypical size and shape compared to appropriately segmented nuclei. Non-viable cells were characterized by positive LIVE/DEAD staining and/or small pyknotic nuclei with extremely bright Hoechst signal. Collectively, the image analysis features that best identified these characteristics included nuclear area and roundness (module: 'Calculate Morphology

Properties'); nuclear Hoechst intensity (module: 'Calculate Intensity Properties'); nuclear LIVE/DEAD stain intensity (module: 'Calculate Intensity Properties'); Hoechst texture features (module: 'Calculate Texture Properties'; SER Features, spot; scale: 4px; normalization by: unnormalized); and LIVE/DEAD texture features (module: 'Calculate Texture Properties'; SER Features; scale: 6px; normalization by: kernel). These extracted features were then used to set filters (i.e., gates) in the module 'Select Population.' In order to exclude extreme outliers representing non-viable or incorrectly segmented cells, filter settings were tuned interactively for each experimental replicate by visually comparing images of cells in DMSO-treated wells against images of cells in active drug-treated wells, and by using histograms produced by Columbus to visualize gates applied to the distribution of measured/calculated values for each feature. Identical gates were applied to all wells on each imaged plate.

Normalized Growth Rate Inhibition (GR) Metrics

Viable cell counts at time=0 and time=72hrs as determined in Columbus were then exported and used to compute GR values and GR metrics with the freely available online GR calculator (http://www.grcalculator.org/grcalculator/), which is based on previously published methods (Hafner et al., 2016). Dose response curves of GR values were produced using MATLAB (MathWorks).

Quantification of Immunofluorescence Images

Immunofluorescence intensities in the entire cell or relevant subcellular compartment were measured in Columbus. Masks for the nucleus, cytoplasm and entire cell were generated by thresholding the Hoechst and the Whole Cell Stain channels. Custom masks were generated for each cell line due to variation in cell morphology. To quantify changes in the levels of proteins/phosphoproteins after treatment with DMSO or active drug, the relevant mask (as determined both by prior knowledge and by the observed staining pattern for each antibody) was applied to microscopy images and the fluorescence intensity was measured in that specific region of each cell. Levels of phospho-AKT (T308 and S473), phospho-4E-BP1 and phospho-GSK-3β in single cells were measured using a whole-cell mask. Phospho-S6 levels were measured using a cytoplasmic mask. Signals for BrdU, EdU, F-ara-EdU, cyclin A2, cyclin D1, FoxO3, geminin, p21, p27, p-Chk1, p-Chk2, p-H2A.X, p-histone H3, p-pRb and p-RPA levels were measured using a nuclear mask. For generation of PI3K signaling heatmaps, background-subtracted fluorescence intensity measurements were first normalized to values for DMSO. The PI3K signaling index was computed by adding the mean DMSO-normalized values of each of nine different proteins/phosphoproteins (scale 0-9, with 9 indicating no difference from DMSO). For signals that increase with PI3K pathway suppression (nuclear FOXO3, nuclear p21, and nuclear p27), the inverse value was used when computing the index. "Percent high" for any measured protein/post-translational modification was determined by applying an identical threshold to the entire distribution of values determined for cells treated with DMSO or active drug (see Figure 4A). Total DNA content and EdU content per nucleus were calculated by multiplying the average nuclear fluorescence intensity by the nuclear area. All raw data were exported from Columbus; visualization, plotting and statistical analysis of the data were performed in MATLAB. Specific gating strategies are illustrated in individual figure panels; experimental replicates and statistical analyses are described in figure legends. Cells with mitotic aberrations were quantified based on visual inspection of individual microscopy images.

Cell-Cycle Analysis and Cell-Cycle-Stage-Specific Immunofluorescence Values

After using Columbus to apply a nuclear mask to individual cells, average Hoechst and EdU intensity values were extracted and multiplied by the nuclear area to determine the DNA content and EdU content, respectively, on a single-cell level basis. The two-parameter plot of nuclear DNA content versus EdU content readily separated cells into three groups representing G1, S and G2/M cells (see Figure S3A). S-phase-non-replicating (S_{NR}) cells were identified based on DNA content intermediate to G1 and G2/M and no EdU signal. The percentages of cells in different cell cycle stages were determined in MATLAB by gating different groups of cells by DNA content (X) and EdU content (Y). In each experiment, specific values for gates were first determined by using data for cells treated with DMSO only and then applied to data for drug-treated cells. For analysis of immunofluorescence intensities in specific subpopulations of cells defined by cell cycle stage (e.g., Figure 2D), nuclear intensity values from cells labeled with Hoechst/EdU and immunostained for a nuclear marker of interest were first plotted in MATLAB using the 3-way scatterplot function to preserve relationships among the three measured intensity values in single cells. Cells in different cell cycle stages were then gated as described above. The entire distribution of immunofluorescence intensity values for cells in each cell cycle stage was then replotted in relation to DNA content.

Live-Cell Analysis of Proliferation and Apoptosis

To determine population growth trajectories, total cell number in an entire well imaged using the 4× lens was determined using Incucyte Zoom software (Essen Bioscience). Cell number was calculated by identifying nuclei positive for GFP (HCC70) or mCherry (Hs 578T, HCC1806) in microscopy images, based on a background-subtracted fluorescence intensity threshold. C3/7-positive cells were similarly identified based on a fluorescence intensity threshold in the GFP channel. For each of three technical replicates in each independent experiment, C3/7 counts over time were plotted and area under the curve (AUC) calculations were determined in MATLAB and averaged. The mean fold-change value was then calculated as the ratio of the average AUC for drug versus the average for DMSO. Plotted mean fold-change and standard error values were determined using data from independent experiments.

Live-Cell Analysis of Drug Effect on the Cell Cycle

Semi-automated tracking of individual HCC1806 cells expressing H2B-mTurquoise and mVenus-hGeminin(1–110) was performed using p53CinemaManual 2.0, a MATLAB-based software package freely available at: https://github.com/balvahal/p53CinemaManual/releases/tag/v2.0.0. Individual cells were tracked in time-lapse movies using nuclear mTurquoise; mVenus fluorescence intensities were then extracted from each tracked cell nucleus. Cell cycle analysis was performed by analyzing plots of mVenus intensity versus time (see annotated trace of a representative single cell in DMSO, Figure 3A). Each individual trace was manually reviewed and compared to DMSO control to ascertain the timing of cell cycle stage transitions. Data for each cell and each condition were then compiled into matrices, which were used to generate heatmaps. Cell divisions were scored by direct visualization of chromosome segregation followed by appearance of daughter cell nuclei. Cell deaths were scored by the appearance of nuclear fragmentation (karyorrhexis).

Analysis of Steady-State Polar Metabolites

Metabolite peak intensities for drug-treated samples were compared to peak intensities for samples treated with DMSO (N=3 independent experiments) using MetaboAnalyst 4.0 (MA) (https://www.metaboanalyst.ca/MetaboAnalyst/faces/home.xhtml). Prior to uploading the data, an initial processing step was performed to exclude metabolites with two or more missing values in either the DMSO or active treatment group. For rapamycin, AZD8055, and Torin2, 34 (11.2%), 35 (11.6%), and 34 (11.2%) of 303 metabolites, respectively, were excluded for this reason. For a small number of excluded metabolites (4/34 for rapamycin, 8/35 for AZD8055, and 9/34 for Torin2), three numerical values were available for DMSO but only 0 or 1 for active treatment, suggesting that treated samples had undetectable levels by mass spectrometry due to low abundance. Because the fold-change values for these metabolites were incalculable but in certain cases could be large, these metabolites and their raw values are listed in separate tables in Table S4. To facilitate downstream analysis in MA, single missing values in either treatment group were imputed by taking the average of the two measured values. This step was performed prior to analyzing the data in MA because the software performs missing value estimation for each metabolite using all of the sample data rather than the data for individual treatment groups. In certain instances, this method was observed to obscure strong changes in metabolite levels induced by drug treatment. Once the data were uploaded to MA, no additional filtering was applied. Sample data were quantile-normalized, and then the metabolite data were log-transformed. No scaling was performed. The effects of data normalization and transformation were visualized using diagnostic plots. Fold-change values were calculated as the ratio between group means, using absolute values of metabolite data prior to log-transformation. T-tests were performed to assess the statistical significance of fold-change values. Volcano plots were generated using fold-change values and p-values from T-tests to identify metabolites with the largest and most significant changes after drug treatment.

DATA AND CODE AVAILABILITY

1. Evaluation of the sensitivity of six TNBC cell lines to 23 PI3K pathway drugs or trametinib (MEK inhibitor). Data summarized in Figures 1B and S1D.
   a. Measured GR values (72 h): the accession number for this dataset is HMS LINCS Database: 20364. Available at: https://lincs.hms.harvard.edu/db/datasets/20364/.
   b. Calculated GR metrics (72 h): the accession number for this dataset is HMS LINCS Database: 20365. Available at: https://lincs.hms.harvard.edu/db/datasets/20365/.
2. Evaluation of the sensitivity of Torin2 compared to the PI3K pathway drugs alpelisib, TGX-221, pictilisib, everolimus, and sapanisertib in a collection of breast cancer cell lines (N=28). Data summarized in Figures 1C and S1E.
   a. Measured GR values (72 h): the accession number for this dataset is HMS LINCS Database: 20343. Available at: http://lincs.hms.harvard.edu/db/datasets/20343/.
   b. Calculated GR metrics (72 h): the accession number for this dataset is HMS LINCS Database: 20344. Available at: http://lincs.hms.harvard.edu/db/datasets/20344/.
3. Evaluation of the sensitivity of HCC1806 and HCC70 cells to Torin1, Torin2, AZD8055 or nine Torin2 analogs. Data summarized in Figures 5B–5C.
   a. Measured GR values (72 h): the accession number for this dataset is HMS LINCS Database: 20366. Available at: https://lincs.hms.harvard.edu/db/datasets/20366/.
   b. Calculated GR metrics (72 h): the accession number for this dataset is HMS LINCS Database: 20367. Available at: https://lincs.hms.harvard.edu/db/datasets/20367/.
4. Targeted metabolomics profiling data (i.e., peak intensity measurements) of BT-549 cells after exposure of to DMSO, rapamycin (1μM), AZD8055 (1μM), or Torin2 (1μM) for 6 hours. Data summarized in Figure 2F. The accession number for this dataset is HMS LINCS Database: 20368. Available at: https://lincs.hms.harvard.edu/db/datasets/20368/.